19. High-Energy Time-Resolved Electron Diffraction

Pietro Musumeci, Renkai Li

This chapter reviews the application of relativistic energy ultrashort electron beams to the direct investigation of structural changes in matter at atomic length scale with sub-picosecond (sub-ps) resolution by time-resolved electron diffraction (ED). There are many benefits of using higher-energy electron beams for time-resolved electron scattering instrumentation, due mainly to the space charge force suppression at relativistic energies, which enables more intense and shorter electron bunches. Speed-of-light probes, higher penetration, and shorter de Broglie wavelength are other advantages associated with MeV electron energy.

The use of MeV beams for electron scattering demands excellent beam quality in both the transverse and longitudinal phase spaces, i. e., an exquisitely high six-dimensional (6-D) brightness. Expertise from the low-energy microscopy and diffraction community has converged with advances made in relativistic electron sources for high-energy particle accelerators and fourth-generation synchrotron light sources in the effort to create and deliver electron beams with these characteristics.

19.1 Ultrafast Electron Diffraction

The use of high-energy electron beams for direct investigation of materials has the ambitious goal of obtaining real-time resolution of atomic motion—one of the grand open challenges in modern science—promising a deeper understanding of the most fundamental processes relevant to the study of molecules, materials, and biological systems. The need to go beyond static pictures and to add the temporal dimension to microscopic investigation has been heeded by a well-timed confluence of a variety of scientific communities, including laser, accelerator physics, and electron microscopy. In recent years, a series of techniques have been developed to follow atomic motion in materials in real time, far from equilibrium [19.1–3].

The range of questions that can be addressed using these techniques includes the study of dynamic phase transformations such as melting and solidification, chemical reactions and elasticity/plasticity phenomena, radiation damage, and shock propagation [19.4]. In condensed matter physics, time-resolved structural dynamics measurements can provide information on electron–phonon coupling and coherent lattice vibration to develop a better understanding of electrical conductivity, for example in graphene and supercon-

P.W. Hawkes, J.C.H. Spence (Eds.), *Springer Handbook of Microscopy*, Springer Handbooks,
https://doi.org/10.1007/978-3-030-00069-1_19

ductors [19.5]. An important application within the field of life sciences is the study of dynamics in complex macromolecules such as proteins, whose function is ultimately set by their temporal evolution behavior. For example, a recent study of myoglobin with 150 ps temporal resolution using x-ray crystallography revealed significant transient conformational changes which could not have been predicted simply by looking at the final and initial states [19.6]. Instruments that can combine very high spatial and temporal resolution have the potential to enable breakthrough advances in the understanding of all of these processes (Fig. 19.1).

The relevant timescale when trying to resolve the motion of atoms and molecules is 100 fs, which is the time required for an atom to move about 1 Å (the typical atomic distance scale). The progress in laser technology has enabled the generation of optical pulses as short as a few fs [19.8]. Nevertheless, ultrafast optical lasers can only provide indirect spectroscopic information on the structural dynamics of samples. Only x-ray photons or fast electrons have sufficient resolution to spatially resolve atomic motion.

There are various schemes for generating short bursts of x-ray or electron beams suitable for ultrafast probing of materials. Many of these take advantage of ultrashort laser pulses to generate the sub-100 fs probe pulses. For a comprehensive review on ultrashort x-ray pulses, see [19.9]. Most x-ray sources, however, require high-energy electron beams, and are expensive and large, as is the case, for example, with modern third-generation [19.10] and fourth-generation x-ray sources [19.11, 12]. Doses involved in these studies are very significant; therefore, obtaining the shortest possible pulse lengths is important, as it allows us to capture the complete structural information from the sample before damage occurs (*diffract and destroy* [19.13]).

Electrons offer a complementary, relatively inexpensive, and effective solution, well suited for smaller laboratories [19.3, 5], to the challenge of studying structural dynamics in real time (i. e., with 100 fs or better resolution). There are important physics differences in the way that electrons and x-rays interact with matter. X-rays are scattered when they cause the atomic electrons to oscillate and re-radiate; electrons are scattered by Coulomb interaction with the atomic nuclei and electrons. Because of the difference by five orders of magnitude between the Rutherford (charged particles) and Thompson (photons) cross sections, an electron

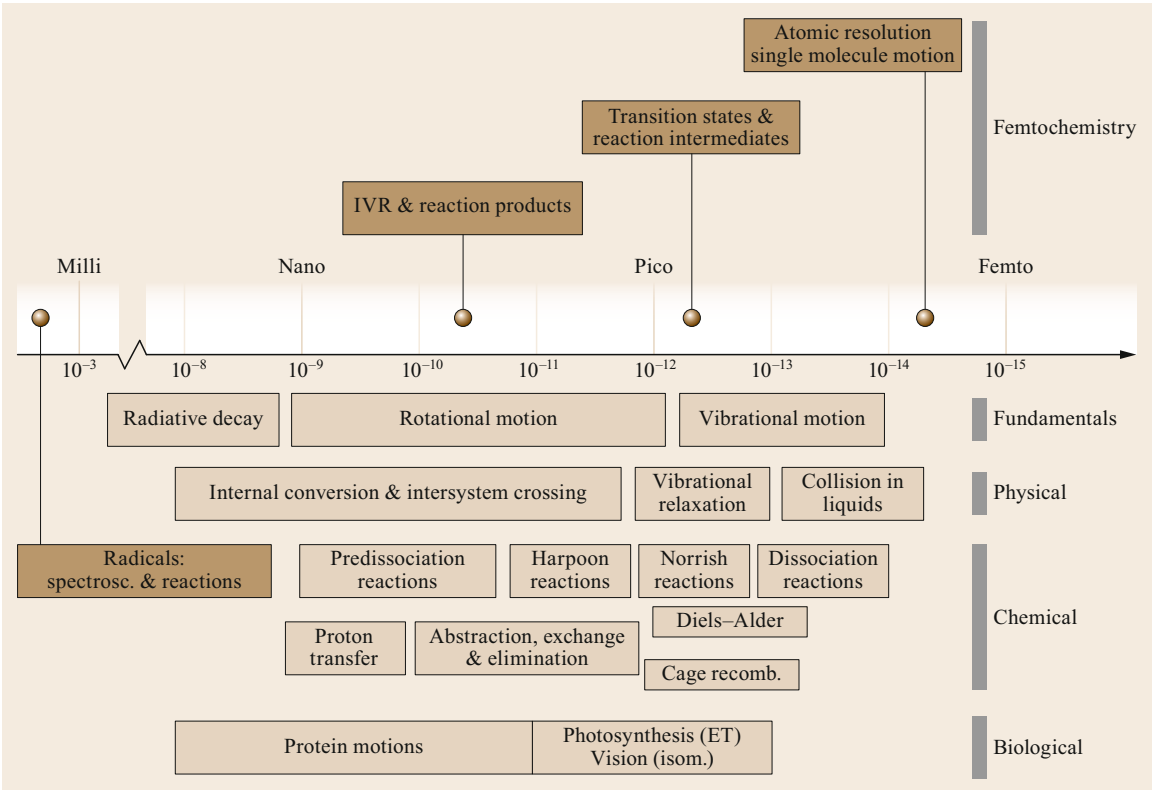

Fig. 19.1 Time scales and their relevance to physical, chemical, and biological changes. Examples are given for each type of change and for each scale. After [19.7]

beam with 10^6–10^7 particles yields the same number of scattered particles as a probe pulse of 10^{12} hard x-ray photons. The stronger interaction of the charged particles makes electrons the preferred choice for the study of thin layers, surface effects, or gas-phase samples, i. e., whenever the number or the density of scattering centers is limited.

Another fundamental difference between x-rays and electrons involves the absorption mechanisms. The inelastic scattering cross section ultimately limits the ability to extract information from the sample, since the number of probe particles can be increased only up to the point where the sample is damaged by the beam [19.14]. For x-rays, the most likely inelastic scattering event is photoelectric absorption, where all of the probe particle energy is deposited in the sample. For hard x-rays (10–20 keV), the total cross section for the photoelectric effect is two orders of magnitude larger than the elastic scattering cross section. For electrons, the energy loss is distributed along different channels, including phonon excitation (a few MeV) and intraband (eV), and collective oscillations (10–20 eV) up to the ionization of core electrons (100–1000 eV). The total inelastic cross section (for low-Z elements), however, is only a few times larger than the elastic cross section, which, combined with the lower deposited energy per inelastic scattering event, makes probing with electrons a much more efficient way to extract information from the target.

A variety of electron scattering techniques, including diffraction, microscopy, and spectroscopy, can be used and adapted for high temporal resolution. The main subject of this chapter is ultrafast electron diffraction (UED), which is without doubt the most mature technique and the one that has produced the greatest number of scientific results thus far.

In conventional UED, an ultrashort electron beam with energy of 30–300 keV is created by illuminating a photocathode with an ultrafast laser pulse. The beam is then accelerated by an electron gun and transported by electron optics to an interaction region. The sample under study is pumped with another laser pulse synchronized at a variable delay to initiate a structural change. A series of diffraction patterns at different time-delay points are acquired. From the analysis of the diffraction patterns, one can retrieve a time-history of the atomic motion in the sample (Fig. 19.2).

In the next section, we will review the historical developments which led to the use of high-energy (MeV) beams for UED, examining the relative advantages (compared to traditional UED) quantitatively. We will then illustrate the key components of a high-energy UED beamline, starting from the electron source, and discuss some of the most common variations in the implementation of this technique, including (i) radio-frequency (RF) streak-camera-assisted continuously time-resolved electron diffraction to capture the sample evolution, and (ii) the application of radio-frequency compression to achieve < 10 fs temporal resolution in MeV electron diffraction.

The first applications of high-energy UED to the study of solid-state and gas-phase systems will be reviewed in Sect. 19.3. Finally, we will outline the ongoing research directions in this field, which include the extension of this technique to sub-μm beam sizes (MeV micro- and nanodiffraction) and the ad-

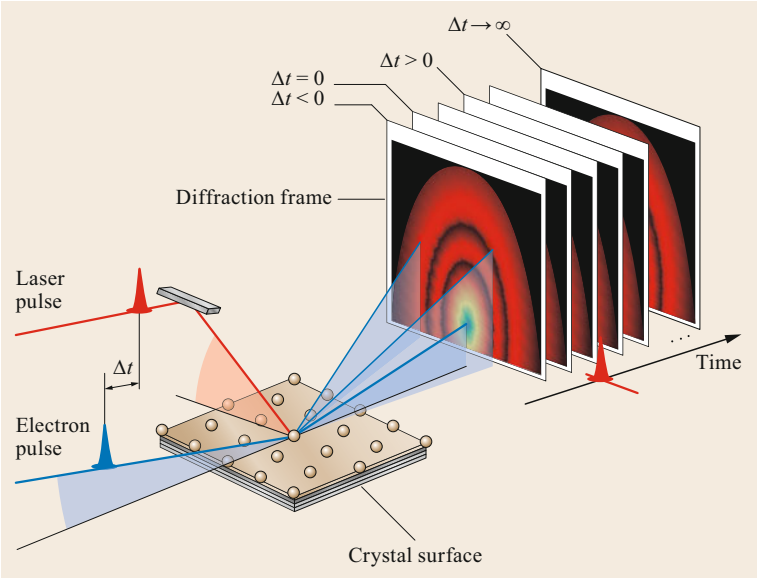

Fig. 19.2 Cartoon schematic of UED technique. A pump laser initiates atomic motion in a sample which is probed by a variable-delay electron pulse. The information regarding the atomic positions is encoded in the diffraction pattern recorded at the detector. Both reflection and transmission geometry can be used for the probe electron beam. Reproduced with permission from [19.15] by John Wiley and Sons

dition of post-sample optics to form images or energy spectrum of the electrons that form the seeds for ultrafast electron microscopy or electron energy-loss spectroscopy.

19.1.1 Background and Historical Development

The use of ultrafast electron bunches to capture diffraction patterns of samples can be traced back to the seminal work of *Mourou* and *Williamson* in the 1980s [19.16]. Their setup was one of the first examples of a photoinjector electron source in which a short laser pulse is used to illuminate a photocathode in an electron gun and generate a synchronized short electron bunch (Fig. 19.3). The beam is then used to capture a series of diffraction patterns from a laser pump at variable delay times, demonstrating for the first time the potential for studying structural dynamics with picosecond temporal resolution [19.17]. It has really been only within the past two decades, due in no small part to the heroic efforts of the *Zewail* group at Caltech [19.18] and the *Miller* group at the University of Toronto [19.19], that UED has graduated to a mature and reliable technique in ultrafast science approaching 100 fs temporal resolution.

The main obstacle to improving the temporal resolution of this technique derives from the fact that conventional UED setups typically employ nonrelativistic electron beams from 30- to 100 keV-photogun direct current (DC) sources, which suffer from severe bunch lengthening and beam quality degradation in the propagation region after the photocathode. This is in part due to the spread in electron velocities from the photoemission process, as previously analyzed in streak camera devices [19.20], but for the overwhelming part dominated by the strong space charge repulsion. At low energy, space-charge-induced broadening in the drift region after photoelectron guns can lengthen the pulse to many times its original length and generate many electron volts of kinetic energy spread in just a few nanoseconds [19.21, 22].

Measures taken to mitigate the degradation of the temporal resolution from these effects include increasing the gun voltage and minimizing the distance from the gun to the sample [19.23–25]. Ultimately, researchers have been able to achieve sub-ps resolution only by significantly reducing the number of electrons (below 10^4 particles per pulse), with the compromise of integrating over multiple shots to collect a single diffraction image. This concept has been taken to the limit of electron bunches with single electrons to completely remove any space-charge-induced effects in the beam dynamics [19.26]. A large number of physical systems have been studied in this way, producing groundbreaking results in the understanding of solid-state phase transitions [19.24, 27], determining the transient species in gas phase [19.28, 29], studying strongly coupled systems [19.30–32], and following surface dynamics [19.33]. The main limitation of this so-called stroboscopic approach is that the process under study must be fully reversible and repeatable for tens of thousands to millions of cycles in exactly the same way in order to accumulate sufficient signal-to-noise ratio in the diffraction pattern.

In order to capture the information concerning the transient structures with a single sub-ps pulse, and hence to enable the study of irreversible phenomena, the highest possible beam intensity must be maintained. Therefore, significant efforts have been directed toward improving the temporal resolution of conventional low-energy UED setups to the 100 fs level [19.34]. Borrowing from standard techniques in high-energy accelerators [19.35], it is possible to reduce the bunch length at the sample using a radio-frequency cavity to impart an energy chirp on the electron beam so that the energy of the tail is higher than that of the front. A short drift section is then sufficient to allow the tail particles

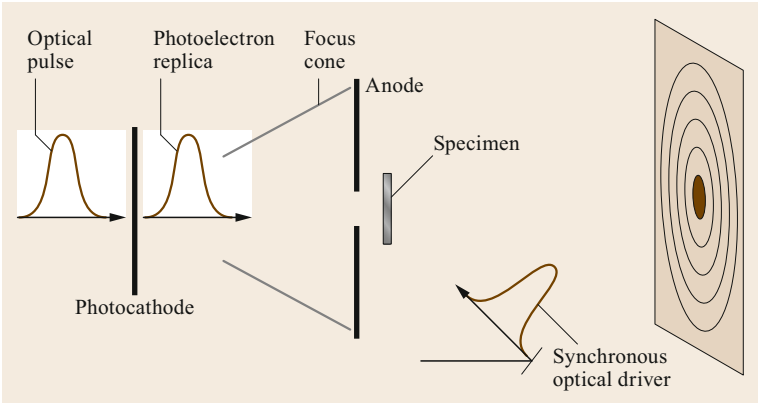

Fig. 19.3 Early setup for picosecond electron diffraction of Williamson and Mourou. After [19.16]

to catch up, resulting in very short bunches. The newest generation of ultrafast diffractometers adopts this technique to push the state of the art of conventional UED below the 100 fs threshold with pulses of hundreds of thousands of electrons [19.36, 37].

The most direct solution for expanding the applicability of UED to the study of irreversible or low-repetition-rate processes, however, is to increase the electron energy to the MeV level, where relativistic effects are able to significantly mitigate the effects of the space charge forces. As early as 1996, in order to solve the space charge problem, *Wang* et al. [19.35, 39, 40] proposed the use of the S-band MeV RF photoinjector as the electron source for UED applications (Fig. 19.4). In the accelerator and beam physics community, this type of electron gun is widely accepted as the state-of-the-art source for high-peak-brightness electron beams, and it is one of the most critical components in the development of short-pulse x-ray free-electron lasers (XFELs) [19.41]. Another important step in acknowledging this possibility occurred with the review paper by *King* et al. [19.4] discussing the evolution of sources for time-resolved diffraction and microscopy, which stimulated the interest of the accelerator community [19.42].

When optimized for UED applications, RF photoinjectors can easily deliver up to 10^7–10^{10} electrons packed in bunches of sub-100 fs length [19.43]. There are two fundamental reasons for the increase of (at least) three orders of magnitude in the number of electrons when using relativistic (3–5 MeV) beams:

- The gradient in an RF photoinjector is 100 MV/m, nearly an order of magnitude larger than that achievable in the conventional UED source, the DC high-voltage diode, or simply the *DC gun*. This ensures that the particles are immediately accelerated to relativistic energies leaving the cathode region, where most of the bunch lengthening takes place.
- As discussed in the next section, space charge forces are significantly reduced as the beam energy increases. Qualitatively, this can be understood by considering the relativistic length contraction effect. In its own rest frame, the electron bunch is very long and has a small charge density; consequently, the electromagnetic forces responsible for the self-repulsion are strongly suppressed.

Following early proof-of-principle work at the Stanford Linear Accelerator Center (SLAC; now SLAC National Accelerator Laboratory), efforts at UCLA [19.43] and Tsinghua [19.44] led to important progress in exploring the feasibility of the technique for characterizing the beam, and demonstrating for the first time the possibility of acquiring high-quality single-shot diffraction patterns using MeV beams from an RF photoinjector.

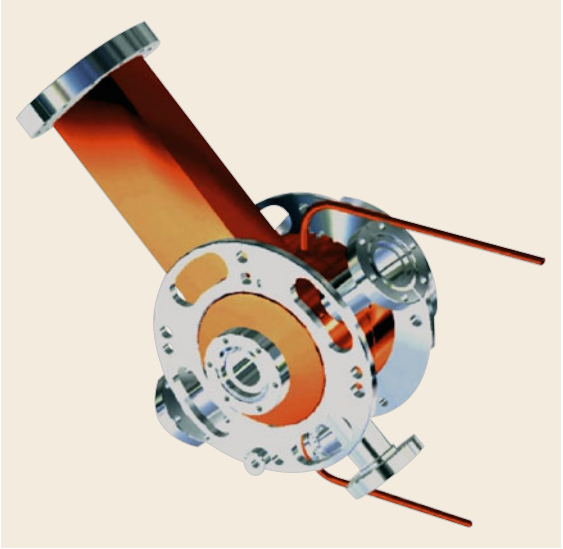

Fig. 19.4 SLAC/UCLA/BNL type S-band 1.6-cell RF photoinjector gun. Reprinted from [19.38] published under CC-BY 3.0 license

Figure 19.5 depicts electron bunch length measurements for nonrelativistic and relativistic electron sources for various charges and initial cathode spot sizes, showing the order-of-magnitude improvements enabled by the high beam energy and greater accelerating field of RF photoinjectors. This work culminated in 2010 with the first application of MeV UED to the time-resolved electron study by single-shot diffraction patterns of ultrafast laser-induced heating and melting of a gold film [19.45].

Setups at Osaka University [19.47] and Brookhaven National Laboratory (BNL) [19.48] soon followed, taking advantage of the superior performance of the MeV UED technique for studies of ultrafast solid-state physics, such as gold and charge-density-wave material dynamics. A more recent development is the REGAE project at DESY Hamburg, which includes an RF buncher in the beamline to obtain ultrashort electron bunches [19.49].

Within the past few years, UED has been recognized as a viable ultrafast investigation tool by both the scientific community and the funding agencies, and a variety of electron diffraction efforts have sprung to life. The most important and successful is the ASTA facility at SLAC [19.50], where gas-phase MeV diffraction was demonstrated for the first time, and thanks

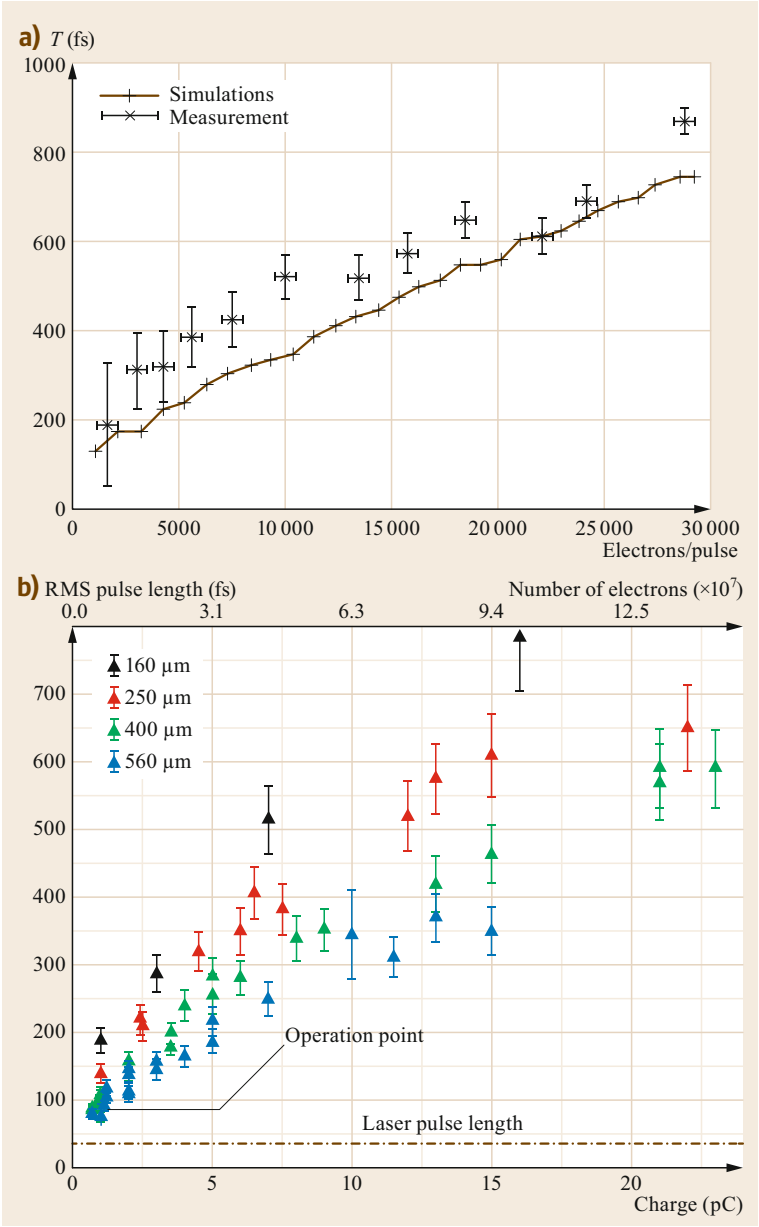

Fig. 19.5 **(a)** Pulse length versus number of electrons for a conventional 60 keV electron gun. Adapted with permission from [19.46], The Optical Society. **(b)** Bunch length versus charge-measured RF at the exit of an RF photoinjector

to the proximity of the Linac Coherent Light Source (LCLS), many users have exploited the complementarity of electrons and x-ray investigation tools. High-repetition-rate MeV UED setups were demonstrated at Beijing [19.51] and Lawrence Berkeley National Laboratory (LBNL) [19.52]. In China, a new setup is being commissioned at Shanghai Jiao Tong University [19.53]. The use of advanced electron sources based on laser plasma accelerators has also found its first applications in UED [19.54].

19.1.2 Advantages of High-Energy Electron Beams for Electron Diffraction Studies

The main advantage of the higher-energy electron beam is the relativistic suppression of space charge forces. In a one dimensional approximation, this can be derived simply by considering the longitudinal equation of motion for an electron in the relativistic regime

$$\frac{\mathrm{d}(m\gamma\beta c)}{\mathrm{d}t} = eE\,, \tag{19.1}$$

where m and e are the mass and charge of an electron, β is the electron velocity normalized to the speed of light c, $\gamma = (1-\beta^2)^{-1/2}$ is the relativistic factor, and E is the electric field generated by the electron charge distribution. We can then use the relation $\mathrm{d}(\gamma\beta)/\mathrm{d}t = \gamma^3 \mathrm{d}\beta/\mathrm{d}t$ to obtain an equation for the acceleration experienced by an electron in the relativistic regime

$$\frac{\mathrm{d}\beta}{\mathrm{d}t} = \frac{eE}{mc\gamma^3} , \tag{19.2}$$

which shows how, for 5 MeV electrons ($\gamma \cong 10$), the same electric field would cause a three-orders-of-magnitude smaller longitudinal acceleration, resulting in a large suppression of the space-charge-induced bunch lengthening. This is the main reason behind the potential for MeV diffraction beamlines to maintain ultrashort bunch lengths for much higher-intensity beams.

The differences between nonrelativistic and relativistic electron beams for diffraction applications are summarized in Table 19.1.

Important advantages of using relativistic energy electrons include:

- A more than three orders of magnitude larger number of particles per pulse, with the potential for acquiring single-shot diffraction patterns and thus enabling the study of irreversible and low-repetition-rate ultrafast processes
- The large accelerating gradients, enabling bunch lengths shorter than 100 fs at the sample
- The relativistic speed of the probe particles, which eliminates the group velocity mismatch problem that degrades the temporal resolution of the technique for thick samples
- The longer penetration depth of MeV electrons, which allows greater variety in sample thickness and geometry. One interesting option yet to be explored is the use of MeV electron diffraction to probe biologically interesting samples dispersed in a liquid contained by electron-thin membranes.

Table 19.1 Comparison between nonrelativistic and relativistic electron diffraction

Parameter	UED (nonrelativistic)	MeV UED (relativistic)
Beam kinetic energy	30–100 keV	3–5 MeV
Accelerating field	10 MV/m	80–120 MV/m
Number of particles per bunch	10^4	10^7
Bragg angle	10 mrad	0.5 mrad
Elastic mean free path (Al)	20–60 nm	200 nm
Normalized emittance	0.1 mm mrad	0.1 mm mrad
Relative energy spread	10^{-5}	10^{-3}
Inelastic mean free path (Al)	43–106 nm	430 nm

Over the years, many challenges that were initially identified as critical for MeV UED have been successfully resolved. These include the poor quality of the diffraction patterns and the lack of very high-efficiency electron detection for MeV ED. We will discuss the detectors later in the technical section of this chapter. Let us analyze the diffraction contrast issue quantitatively.

We can start by defining the de Broglie wavelength associated with an electron of momentum $p = mc\beta\gamma$, $\lambda = h/p$, where h is the Planck constant. For 4 MeV electrons, $\lambda = 0.3$ pm. For a typical interatomic distance $d = 2$ Å, the Bragg angle is only $\theta_\mathrm{B} = \lambda/d = 1.6$ mrad (as a comparison, for a 30 keV beam, $\lambda = 25$ pm and $\theta_\mathrm{B} = 35$ mrad). In order to distinguish the scattered particles from the undiffracted beam core, θ_B must be much larger than the intrinsic root mean square (RMS) spread in beam divergence angles at the sample σ_θ—i. e., $\sigma_\theta \ll \theta_\mathrm{B}$.

It is important to realize here that relativistic electrons have a much shorter de Broglie wavelength and therefore scatter at significantly smaller Bragg angles than their nonrelativistic counterparts. Therefore, when considering the finite point spread function (PSF) of the detection system, a longer distance between the sample and the detector is needed in order to spatially resolve the Bragg peaks from the main central beam.

An equivalent way of looking at this is by introducing the concept of the transverse coherence length. Transverse coherence length is defined as $L_\mathrm{c} = \lambda/2\pi\sigma_\theta$, and it has to be compared with the structure interplanar distance d. If the beam is not coherent over a few unit cells of the observed structure (i. e., $L_\mathrm{c} > d$), then no constructive interference can be obtained, and the visibility of the diffraction peaks is strongly reduced. For an electron beam at a waist

$$\sigma_\theta = \frac{\epsilon_\mathrm{n}}{\sigma_x \beta\gamma} , \tag{19.3}$$

where ϵ_n is the normalized beam emittance, a conserved quantity in linear electron transport. This implies that the coherence length L_c or, equivalently, the figure of merit for diffraction contrast $\sigma_\theta/\theta_\mathrm{B}$ is independent of the beam momentum or energy.

Another important difference is related to the differential cross section $\mathrm{d}\sigma/\mathrm{d}\Omega$ for the interaction of higher-energy particles with matter. Following *Salvat* et al. [19.55, 56], for elastic scattering from an atom with atomic number Z, we can write

$$\frac{\mathrm{d}\sigma}{\mathrm{d}\Omega} = \frac{4Z^2}{s^4 a_0^2} \frac{1-\beta^2 \sin^2\frac{\theta}{2}}{1-\beta^2} (1-F(s)^2)^2 , \tag{19.4}$$

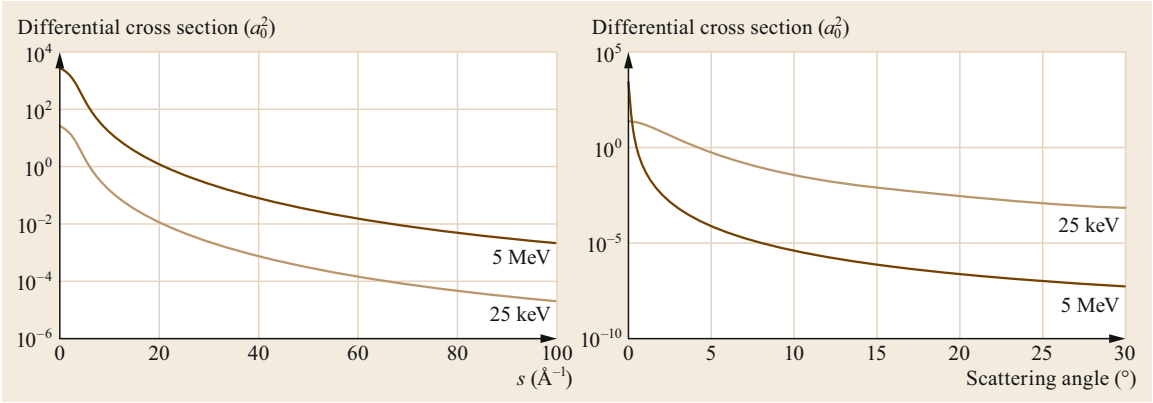

Fig. 19.6 Differential elastic scattering cross section (in units of the atomic Bohr radius a_0^2) versus momentum transfer and scattering angle for 25 keV and 5 MeV electrons

where a_0 is the atomic Bohr radius, $s = 4\pi/\lambda \sin\theta/2$ is the momentum transfer, and $F(s) = \sum_i A_i\alpha_i^2/(s^2+\alpha_i^2)$ is a function which depends on the details of the atomic potential. For example, for silver, $A_i = 0.25, 0.62$, and 0.13, and $\alpha_i = 15.59$, 2.74, and 1.14 Å^{-1}. When plotted versus the momentum transfer, the differential cross section is larger by a factor of γ^2 for MeV electrons (Fig. 19.6). In order to calculate the number of scattered electrons in a given solid angle, however, we need to integrate over the scattering angle and not in s. The result for the total cross section then shows that the number of scattered electrons is 5–10 times lower for 5 MeV than for 100 keV over the relevant momentum transfer range, corresponding to the differences in elastic mean free path quoted in Table 19.1.

The total inelastic cross section depends on the electron energy as the inverse square of the relativistic velocity factor (i. e., $\propto \beta^{-2}$), and therefore the inelastic/elastic ratio is nearly energy-independent [19.5, 57]. The scaling as a function of the atomic number Z is more complex, as it depends on the outer-shell structure of the element and the available channels for energy exchange. The ratio of inelastic to elastic cross section decreases, and is approximated as C/Z, where $C \simeq 18$ [19.7].

For crystalline samples, the very short wavelength associated with high-energy electrons provides an advantage in terms of the intensity of the diffraction signal for high-order Bragg peaks. This is because the corresponding Ewald sphere is extremely flat and can satisfy the Laue condition for many reciprocal lattice points. Assuming kinematic diffraction (i. e., sample thickness smaller than a few mean free path lengths), the diffracted intensity can be written as the product of the structure form factor, which contains the details of the unit cell atomic composition and structure, and the lattice amplitude G [19.58], which is dependent on the external shape of the crystal. For a sample with N crystal planes spaced at distance d, we have

$$G^2 = \left[\frac{\sin(\pi\Delta kNd)}{\pi\Delta kd}\right]^2, \qquad (19.5)$$

where $\Delta k = 4\pi/[\lambda(1-\cos\theta/2)]$ is the deviation from the perfect Laue condition. The lattice factor shows the characteristic Bragg enhancement factor of up to N^2 when the Ewald sphere exactly crosses the reciprocal lattice point (i. e., $\Delta k = 0$). Because of the much smaller wavelength and scattering angles, for $N = 100$ and $d = 4$ Å we can calculate that G^2 for 100 keV electrons is nearly 1000 times smaller than for 5 MeV electrons (Fig. 19.7). Especially for thick samples where the reciprocal lattice points are very well defined, this offers an important advantage in terms of scattering efficiency for Bragg peaks of very high order.

Another point that has been raised against the use of high-energy electrons for probing biological materials is related to the knock-on damage effect. This effect was primarily responsible for the progressive disappearance of high-voltage (MeV) electron microscopy. In high-energy UED, this problem is completely avoided, due first of all to the much lower dose required to acquire a diffraction pattern. Furthermore, the diffraction signal

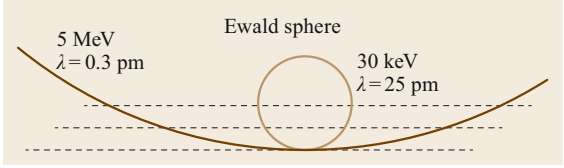

Fig. 19.7 Ewald sphere construction for 100 keV and 5 MeV electrons. The reciprocal lattice spacing is set by crystal lattice constants. By changing the crystal thickness, the magnitude of this effect can be controlled

can be acquired well before any structural change due to damage (i. e., in a few tens of femtoseconds), in an approach similar to the diffract-and-destroy technique employed in fourth-generation light sources [19.13]. The prospects for outrunning the damage in electron diffraction were recently analyzed [19.59].

19.2 High-Energy Time-Resolved Electron Diffraction Instrumentation

High-energy ultrafast electron scattering techniques have many important components, all of which must be well integrated to maximize instrument performance. The key elements of a high-energy beamline for direct material investigation include the following: an ultrafast laser that is used to both generate the electrons and initiate atomic motion in the sample, an electron gun to provide the initial acceleration, electron optics and collimation, before the sample to provide the proper illumination condition and after the sample plane for magnification and energy analysis, and transverse and longitudinal beam diagnostics to assist in tuning the beam propagation through the column (see Fig. 19.8).

In order to achieve higher field gradients and maintain a compact setup, the use of RF cavities for the initial acceleration is preferred over static DC voltage, due to the higher breakdown threshold for high-frequency fields. The beam is typically generated by illumination of a photocathode embedded in the electron gun using an ultrashort laser pulse. The photoemission process requires special attention since, as we will later see, it plays a critical role in determining the beam brightness. RF fields can also be applied downstream of the gun to manipulate the beam longitudinal phase space—for example, imparting a strong energy chirp to make the arrival times of the electrons nearly equal at a given plane (velocity compression) or to minimize the beam energy spread when very monoenergetic probe beams are desired. Another approach involves the use of an RF deflecting cavity to streak the beam after its interaction

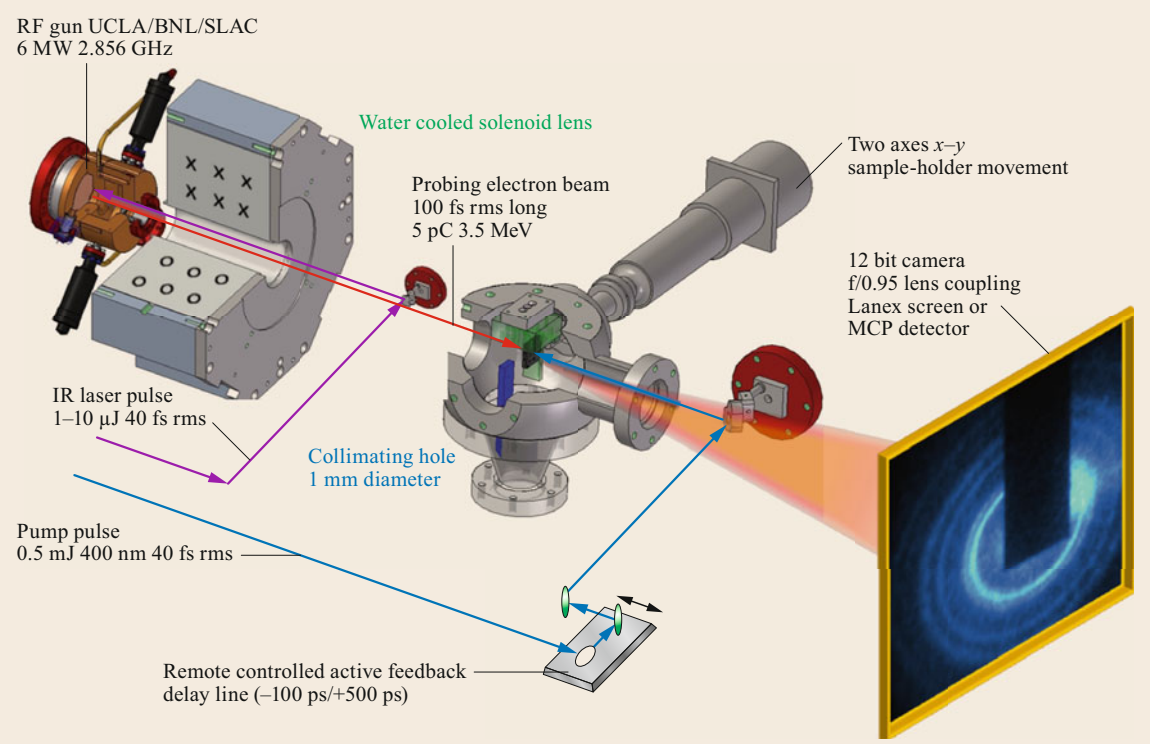

Fig. 19.8 Relativistic beamline for ultrafast electron diffraction. Elements of a relativistic UED beamline. A laser pulse strikes a cathode inside an electron gun to liberate a short pulse of electrons. These are accelerated to high energy by the radio-frequency fields. The solenoid focuses the beam from the RF gun and allows diffraction patterns to be captured, such as the one shown in the figure

with the sample so that it becomes possible to visualize the entire time-history of the ultrafast process under study in a single shot.

Efficient detectors are employed to extract the information from the beam phase space distribution after interaction with the sample, and advanced beam diagnostics in general are essential for beam tuning and optimization. This is an active area of research, as the high-brightness, low-charge beams employed in electron scattering applications at relativistic energies challenge the state of the art of beam diagnostics in both spatial and temporal resolution.

In order to design and optimize the electron beamline for relativistic UED/UEM, particle-tracking simulation codes that have been well-benchmarked with experimental results can be reliably used. These codes can push the particles in the fields of each beamline element while at the same time keeping track of interparticle interactions. Modeling of space charge is usually done using smooth mean field models, but for the most advanced cases, when computational power permits, it is also possible to take into account binary electron–electron interactions.

In the following, we discuss all of these critical components, their technical development status, and their impact on high-energy electron diffraction instrumentation.

19.2.1 UED Beam Brightness Requirements

Let us start from some general considerations regarding the beam quality required for this application. In practice, the demands on the beam parameters for UED depend largely on the process under study. The number of electrons determines the signal-to-noise ratio in the diffraction pattern. The milestone time-resolved electron diffraction results on Al melting were obtained using 150 shots of 6000 electrons each, for a total of 1 million electrons per image [19.24]. This can be considered a good estimate for the minimum charge per bunch required to obtain a high-contrast diffraction pattern. Beam charges of interest range from a few pC for obtaining a high-contrast full-field image in transmission electron microscopy mode, down to < 10 fC for multishot diffraction patterns of fully crystalline specimens, where the Bragg enhancement can provide orders of magnitude increase in the signal (Fig. 19.9).

The probability of elastic scattering for each electron in the beam is described by a Poisson distribution with an expectation value equal to the ratio of the thickness of the sample to the elastic mean free path. In practice, the amount of charge required for a time-resolved study depends on the magnitude of the changes in the diffraction pattern. The statistical fluctuations as a result of the discrete nature of the probe particles in the intensity of the Bragg peak (shot-noise) determine the noise floor and should be kept much smaller than the amplitude of the expected signal. For example, if a 1% amplitude drop for a Bragg peak is expected after the pump laser illuminates the sample, at least 40 000 particles in the Bragg peak are required to have a 2 : 1 signal-to-noise ratio. This number drops by a factor of 100 if the signature of the time-dependent effect is 10% or larger. In other words, the beam charge is fixed by the requirement of having enough scattered electrons to obtain good statistics on the diffraction peak parameters

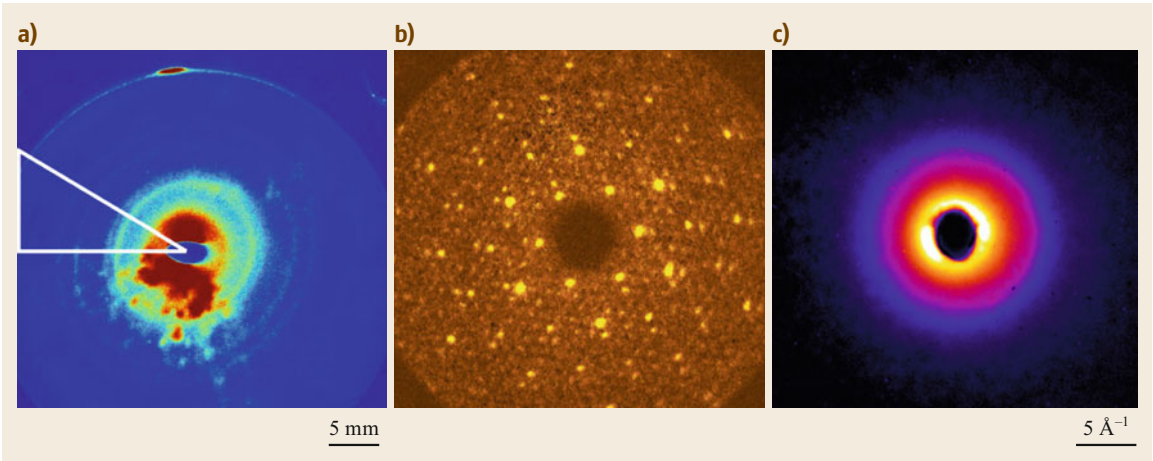

Fig. 19.9a–c MeV diffraction patterns on different samples. **(a)** Single-shot Al diffraction pattern obtained with 10^6 electrons. Reprinted from [19.44], with the permission of AIP Publishing. **(b)** Single-shot diffraction pattern of charge density wave crystal 1T-$TaSe_2$ obtained with 5×10^4 electrons. From [19.48] published under CC-BY 3.0 license. **(c)** Gas-phase diffraction pattern using 10^9 electrons. Reprinted from [19.50], with the permission of AIP Publishing

that are being tracked as a function of time. Obviously, it is always possible to average over multiple images and distribute the charge over multiple electron pulses, but for the sake of the discussion here, all the electrons are in one pulse, as single-shot diffraction patterns are one of the main advantages of high-energy UED.

Aside from charge, peak current and bunch length are also very important parameters, as they determine the number of electrons within the relevant measurement time (ranging from sub-ps to tens of fs) for observing dynamic changes in the diffraction patterns [19.43]. The temporal resolution of a UED instrument can be written as

$$\Delta t = \sqrt{\Delta t_{\mathrm{e}}^2 + \Delta t_{\mathrm{vm}}^2 + \Delta t_{\mathrm{l}}^2 + \Delta t_{\mathrm{jitter}}^2}\,, \tag{19.6}$$

where Δt_{e} and Δt_{l} are the electron and laser pulse lengths, respectively; Δt_{vm} is the so-called velocity mismatch term, which is dependent on the difference in velocity between the probe and pump pulses and the thickness of the sample; and $\Delta t_{\mathrm{jitter}}$ is related to the uncertainty in the relative delay of the pump and probe pulses. In most cases, the length of the electron beam is the main contribution to this quadrature sum, and it generally needs to be shorter than or comparable to the fastest observable timescale in the system.

In terms of transverse quality, the electron beam spot size at the sample plane must be fairly small, due mainly to the typical size of the thin samples required to operate in transmission mode. Another issue limiting the transverse extent of the probe beam is related to the requirements for the pump laser fluence. With a limited amount of energy per pulse available from the laser system, the laser pump spot size on the sample typically must be sub-mm to reach fluences of interest for irreversible material processes ($0.01-1\,\mathrm{J/cm^2}$). In order to ensure that the probe beam sees a uniformly pumped area, its spot size should be much smaller. For all of these reasons, the spot size at the sample must be kept at or below 100 μm. When combined with the requirement that the intrinsic beam divergence should be smaller than the typical Bragg angle (on the order of 1 mrad for relativistic electrons), this implies a normalized emittance limit of $\epsilon_{\mathrm{n}} < 100\,\mathrm{nm}$.

We can quantify these statements by calculating the resolving power of the diffraction camera in the case of powder diffraction [19.60]. This quantity is defined as $\mathbb{R} = R/\Delta R$, where R is the radius of the diffraction rings on the detector screen, and ΔR is the smallest distance between two neighboring rings that can simply be discriminated. It is dependent on both this thickness of the ring and the point spread function (PSF) of the detector. A typical electron microscope diffraction camera achieves $\mathbb{R} = 10^3$ or more for static images. For high-energy UED, a resolving power of $\mathbb{R} > 10$ guarantees a good-quality diffraction pattern and provides enough spatial resolution to adequately resolve typical ultrafast structural rearrangements. With a proper choice of beam optics, it is possible to image the angular distribution on the screen and obtain $\mathbb{R} = \lambda/2d\sigma_\theta$. Since $\sigma_\theta = \epsilon_{\mathrm{n}}/\beta\gamma\sigma_{x0}$, where σ_{x0} is the spot size at the sample, we can write

$$\mathbb{R} = \frac{h}{2m_0cd}\frac{\sigma_{x0}}{\epsilon_{\mathrm{n}}}\,. \tag{19.7}$$

Note again that even though the de Broglie wavelength λ for a 4 MeV electrons is > 20 times shorter than that for nonrelativistic particles, the coherence length and the resolving power of the diffraction camera depend only on the normalized emittance of the source, and are in fact independent of the beam momentum. In order to keep $\mathbb{R} > 10$ with a wavelength $\lambda = 0.3\,\mathrm{pm}$ and $d = 2\,\text{Å}$, it is necessary to have at the target $\sigma_\theta < 0.08\,\mathrm{mrad}$. For relativistic electron diffraction, this angular spread (which is ultimately due to the finite beam emittance) is the limiting effect on the diffraction camera resolving power. The contribution from the rms beam energy spread $\delta\gamma/\gamma$ is typically smaller. For example, a beam with a relatively large energy spread $\delta\gamma/\gamma = 1\%$ would still yield diffraction patterns with large contrast $\mathbb{R} = R/\Delta R = \gamma/\delta\gamma > 100$.

A state-of-the-art UED beamline, such as the one at the ASTA facility at SLAC, typically runs a 60 fC (4×10^5 electrons per pulse) electron beam of 3.7 MeV beam energy, with normalized emittance of 18 nm and 100 fs bunch length for stroboscopic (multi-shot) diffraction [19.50].

At this point it is useful to understand the limit of beam brightness for ultrafast electron sources. Various expressions can be found in the literature for the scaling of the brightness, and in particular its dependence on the launch field, which is the accelerating field seen by the particles as soon as they are emitted. It will be helpful here to briefly review them. The first clarification involves the definition of brightness one adopts [19.61]. Common choices among electron source practitioners include four-dimensional (4-D) and five-dimensional (5-D) brightness. Some authors have introduced 6-D brightness as the more fundamental Liouville volume, but the scaling of this quantity with the injection field is more complex, as it involves the effect of intrabeam scattering (Boersch effect [19.62]) and has not yet been discussed in detail in the literature. Moreover, because of the experimental challenges in the measurement of the longitudinal phase space [19.63], 6-D brightness finds less practical relevance at this time.

The 4-D brightness is defined simply as the charge density in the 4-D transverse phase space. The actual

scaling of 4-D brightness as a function of the field depends on the emitted beam aspect ratio at the cathode. If the beam is very short in the longitudinal direction and can be approximated as an infinitely wide thin disk of charge, the emission is cut off at the moment the surface charge density (divided by ϵ_0) equals the accelerating field E_0, and one can write the limit for the achievable beam brightness as

$$B_{\mathrm{n,4D}} = \frac{mc^2\epsilon_0 E_0}{2\pi k_{\mathrm{B}} T} , \tag{19.8}$$

where $k_{\mathrm{B}}T$ is the mean transverse kinetic energy resulting from photoemission (typically on the order of the difference between the photon energy and the cathode work function) [19.64].

When transverse effects are taken into account, and we can no longer approximate the beam as an infinite charged plane, as electrons are accelerated away from the cathode, their contribution to the space charge field at the cathode will decrease, and the emitted charge in this regime scales as $E_0^{1.5}$ [19.65]. The aspect ratio of the laser illuminating the cathode is one of the main levers for the trade-off of transverse emittance at the expense of electron bunch length. In most cases, in order to generate the shortest possible electron beams and maximize the temporal resolution, MeV UED setups use a fairly wide aspect ratio on the cathode, with laser pulses of 100 µm spot size by 45 fs pulse lengths. Genetic optimization algorithms have also been employed to optimize the dimensions of the laser on the cathode [19.66].

For the sake of completeness, another frequently used definition worth mentioning is the 5-D brightness, which is relevant for the FEL gain length optimization, and it is defined as the current density in the 4-D phase space, and therefore equal to the 4-D brightness divided by the pulse length. In the one-dimensional (1-D) approximation, and for a space charge field much lower (< 10%) than the accelerating field but still large enough to cause strong debunching (expansion) of the electron beam, the final pulse length is dependent on the accelerating gradient, and the maximum achievable peak brightness scales as E_0^2 [19.67, 68].

For 5×10^4 electrons with a bunch length of 100 fs, an angular divergence of 0.08 mrad, and an rms beam size of 0.2 mm at 4 MeV energy, the source has to be able to generate a state-of-the-art beam with normalized brightness of $B = 2I/\epsilon_{\mathrm{n}}^2 > 10^{15}\,\mathrm{A/m^2}$. To give a sense of the order of magnitude of this brightness, the RF photoinjector source for the LCLS x-ray FEL generated beams of 20 pC, 0.13 mm mrad emittance, and 5 ps bunch length, with brightness of $\approx 4.5\times 10^{14}\,\mathrm{A/m^2}$ [19.69].

19.2.2 Gun Technology

Most groups active in MeV electron diffraction [19.15, 70] have adapted existing electron guns originally developed for other applications to electron diffraction or microscopy. Interestingly, very few attempts have been made to develop electron guns targeted to these applications. This is most likely because of the long research and development lead time required for a completely new electron gun design and the relative novelty of this application, which only in the last 5 years has gained the full attention of funding agencies. However, it is also indicative of the flexibility of the existing RF photoguns, which, even though initially designed for FEL or advanced accelerator applications [19.71], have been working well in the new parameter regimes required by MeV UED.

The workhorse for high-energy UED has been the S-band RF gun of the UCLA/SLAC/BNL type. Accelerating gradients as high as 120 MV/m and output energy of > 5 MeV are possible using this gun, which is typically driven by up to 10 MW of 2.856 GHz power. In terms of setup size, the gun itself is < 10 cm long, but the high-power system to feed it (typically a modulator–klystron assembly) can be much bulkier.

As the particles are borne at very low velocity, they slip back in the RF wave so that the optimal launch phase is around 30° in the sinusoidal oscillation (where 0° corresponds to the field switching sign at the cathode), which effectively reduces the field at injection by a factor of 2. Also, because of cooling and available RF power, this type of gun is typically run at a low repetition rate (100 Hz has been demonstrated, but < 1 kHz seems feasible with current technology). The low repetition rate limits the average current and the bandwidth available for feedback systems. For these guns, stability in the high-power RF amplitude and phase is one of the main concerns. The state of the art achieves $< 10^{-4}$ relative amplitude jitter and < 0.05° phase jitter [19.72].

Modifications of the standard S-band gun include the so-called hybrid gun, where the standing wave portion of the gun is immediately followed by a traveling wave to compress the bunch [19.73, 74] (Sect. 19.2.6) and the 1.4 cell gun [19.75], where the optimal injection phase is > 70° to maximize the launch field. Advanced material solutions such as the use of hard copper [19.38] or cryo-cooled copper [19.68] are promising in terms of pushing the limits of accelerating field, but have not been demonstrated in operating environments.

For higher repetition rates, a variety of solutions are available. Originally developed for the high repetition rate FELs [19.76], the 186 MHz APEX gun recently demonstrated high-quality diffraction patterns

using sub-ps electron bunch lengths [19.52]. The peak accelerating field on the cathode is 20 MV/m, and the output kinetic energy is 750 keV. The main advantage here is the possibility to operate at MHz repetition rates and therefore achieve a very large flux of probe electrons on the sample. Plans have been made to double the final energy and increase the gradient on the cathode to 34 MV/m.

Superconducting RF (SRF) guns and more exotic solutions (DC guns + superconducting booster cavities) have been proposed [19.51], but so far have only produced static diffraction patterns and thus require additional research. The main advantage of using superconducting RF technology is the possibility of achieving higher field gradient and 2–3 MeV output energy, while preserving the very high repetition rates of the APEX gun [19.77].

We should also mention the possibility of using advanced accelerator concepts such as laser wakefield acceleration (LWFA) to generate the electron beams for high-energy UED. In the past decade, there has been great progress in plasma-based techniques for accelerating particles [19.78]. Here, an ultra-intense laser pulse drives a relativistic electron density wave in a plasma. The result is a relativistic accelerating structure with an extremely high accelerating gradient, in the order of 100 GV/m, which is able to accelerate electrons to relativistic energies in micrometer distances. Currently, laser plasma accelerators provide electron beams ranging from hundreds of MeV to multi-GeV energies, and charges in the range of tens of pC. Numerous methods have been developed to control the injection of electrons into the wakefield, resulting in energy spreads of a few percentage points. In addition, when the injection is done properly, fs electron bunches can be generated: in [19.79], an 80 MeV electron beam with 1.5 fs rms duration was experimentally demonstrated. This emerging technology holds the promise of compact particle accelerators delivering high-charge fs bunches with intrinsic synchronization to an optical pulse [19.80]. Jitter-free synchronization originates from the fact that the accelerating structure is directly driven by the laser. Therefore, temporal jitter arises only as a result of the energy-dependent time of flight from the source to the sample, and sub-10 fs temporal resolution should be attainable in experiments. Diffraction patterns have been recorded using laser plasma accelerator sources, demonstrating the feasibility of the approach [19.81].

Examples of above mentioned various types of electron sources for UED are shown in Fig. 19.10 and their main parameters are summarized in Table 19.2.

Table 19.2 Parameters for various electron guns used for high-energy UED

	S-band gun	VHF gun	SRF gun	LWFA gun
Gradient	60 MV/m	20 MV/m	40 MV/m	> 1 GV/m
Output energy	5 MeV	0.75 MeV	4 MeV	3 MeV

19.2.3 Photocathodes

The electron beam is typically generated by illuminating a photocathode embedded in the gun with an ultrashort electron pulse [19.82]. Photoemission sources can generate beams of low transverse momentum with high charge and with a pulse length and format easily controllable by the laser, which is usually synchronized with the pump pulse that will initiate motion in the sample. Laser technology has advanced to the point where laser pulse shaping can be used to provide full control of the beam distribution [19.83].

Given the brightness scaling of (19.8), it is clear that a fundamental limiting element for electron beam sources is the photoemission physics which contributes the initial energy of the electrons $k_B T$. Electrons emitted from the cathode can be manipulated in 6-D phase space, but the intrinsic quality of the electron beam is fixed once the electrons leave the cathode surface. Therefore, a key aim of modern beam physics is understanding and improving the quality of the electron beam from the cathode itself.

Photocathodes are characterized by the intrinsic divergence, which is defined here as the initial cathode emittance per unit rms laser spot size on the cathode, or in other words, the angular spread of the electrons as they leave the cathode surface. This quantity is equal to the mean transverse energy (MTE) distribution of emitted particles, i. e., $\sqrt{\mathrm{MTE}/(m_0c^2)}$. The scale for the MTE is the difference between the energy of the laser photons and the effective work function of the material which can be modified by the large electric field of the gun (Schottky effect). Metal cathodes currently used in XFEL or UED beamlines typically have on the order of 300–500 MeV MTE and 0.75–1 mm mrad/(mm rms) normalized intrinsic divergence values.

Cathodes for high-brightness electron sources can be common metals or semiconductors. For metal cathodes, *Dowell* and *Schmerge* [19.84] highlighted the links between the quantum efficiency and the MTE. Metals are known for their ruggedness and can operate in a moderate vacuum (10^{-6}), and they are prompt emitters. The cathode time-response is relevant to ultrafast electron scattering techniques, because in the absence

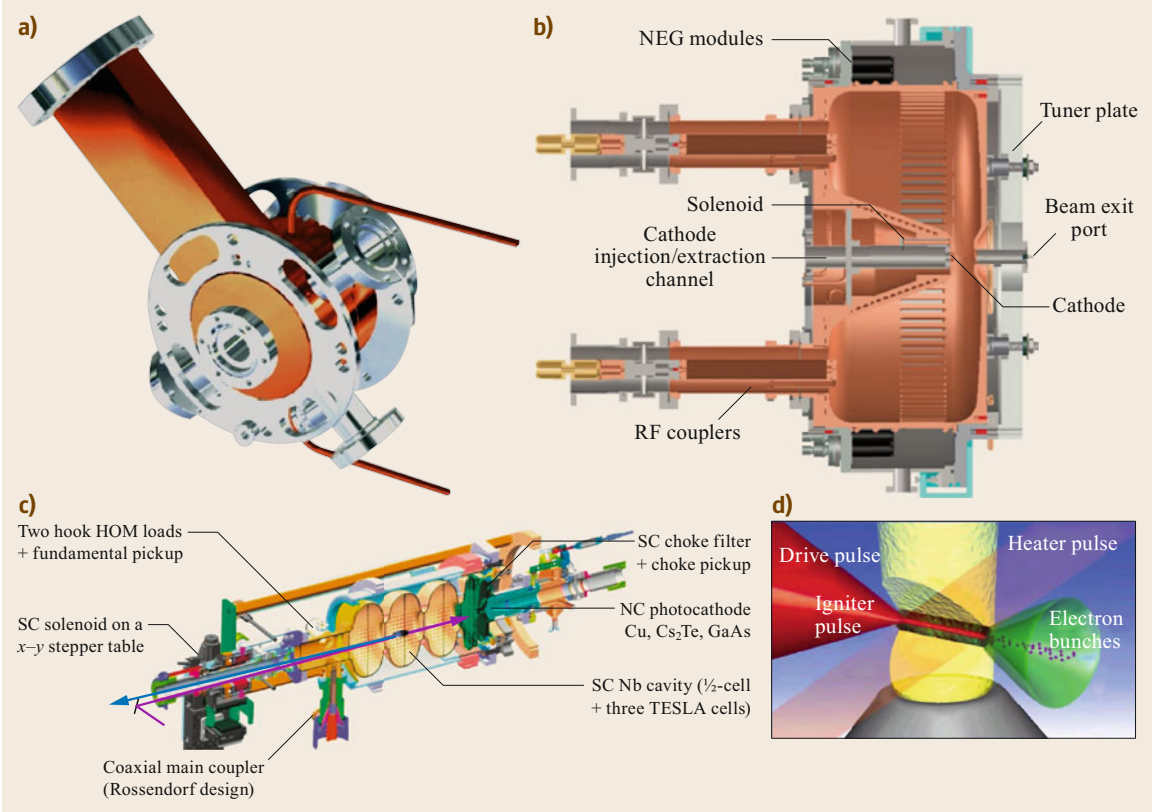

Fig. 19.10a–d Quad chart with (a) S-band 1.6 RF gun (reprinted for [19.81] and published under CC-BY 3.0 license), (b) LBNL APEX gun (from [19.76] published under CC-BY 3.0 license), (c) SRF gun (from [19.70] published under CC-BY 3.0 license), (d) LWFA injector (courtesy of Win Leemans, Lawrence Berkeley National Laboratory)

of longitudinal beam compression, this is the quantity that limits the duration of the electron bunches.

In order to improve (i. e., minimize) intrinsic divergence, research is focused on reducing the MTE of the emitted electrons through the use of oriented single-crystal materials in which the electron band structure is used to minimize transverse momentum. It is also possible to tune the laser energy just above the threshold for photoemission, but in this case the yield is significantly reduced [19.85]. In order to compensate for the lower yield, more photons can be used to illuminate the cathode, but it has been suggested that at some point, the laser energy heats up the electronic distribution in the cathode, negating the possibility of emitting a cold electron beam [19.86]. The emittance can also be drastically increased by nanoroughness and minute changes in surface potential [19.87].

Semiconductor cathodes hold promise for much lower intrinsic divergence, and considerable research efforts over the past few years have been devoted to exploring the emission characteristics of certain classes of semiconductors, such as alkali antimonides. Recent results of cryo-cooled cathodes have shown MTE as low as 20 meV [19.88]. For another class of semiconductor cathodes (III–V class), such as GaAs, the possibility exists to generate spin-polarized electrons [19.89]. These cathodes all typically require a very high vacuum (better than 10^{-9} Torr) and have not yet been tested in the highest-energy UED guns.

For even lower beam charges, brightness scaling laws confirmed by numerical optimizations indicate that sub-micrometer source sizes would be ideal for such applications. These can be achieved either by restricting the physical dimensions of the emitter or by focusing the laser with a high-numerical-aperture optical system to diffraction-limited spot sizes. For example, the laser can be focused from a special oblique incidence port in the gun or, for transmission-mode cathodes, even from the cathode backplane to minimize the distance between the last optical element and the photocathode [19.90]. The resulting smaller emittance not only improves the beam transverse quality, but it also enables the production of shorter bunch lengths by reducing the time-of-flight differences for particles

at different radial offsets in bunching schemes [19.91], while minimizing the transverse effects on the bunch length measurement in deflecting cavities [19.92].

19.2.4 Collimation

An important element that was found to significantly improve the spatial resolution and signal-to-noise ratio in diffraction patterns was the introduction of a collimating pinhole aperture before the sample plane. The dimensions of the hole are optimized to permit a sufficient number of particles to pass through in order to preserve the ability to record the diffraction pattern in a single shot.

Without the collimator, the dimensions of the probe beam depend on the beam dynamics and are sensitive to many operating parameters. With the use of a fixed aperture, the probe area has a well-defined size, facilitating matching to the pump beam and alignment. Other advantages of collimation including the removal of dark-current background resulting from unsynchronized field emission, which constitutes a large source of noise in relativistic UED patterns, especially for very high-gradient electron guns. The collimator can also be used to separate the high-vacuum region of the electron gun from the sample region. This is very important when differential pumping systems are required, such as in gas-phase studies.

Most importantly, the solid curve in Fig. 19.11 shows the transverse beam spot size when the beam charge extracted from the cathode is 10 pC, with an initial laser spot size of 500 μm, and a collimating hole is used. The collimated beam charge hitting the sample is 1.6 pC. The spot size at the screen is almost three times smaller than what we would achieve without the hole. Since $\mathbb{R}$ is inversely proportional to the spot size at the detection screen, this is a significant improvement in spatial resolution. To give an idea of the importance of this, we note that to resolve the ⟨111⟩ and ⟨200⟩ rings in the Debye–Scherrer pattern of polycrystalline gold, $\mathbb{R}$ has to be larger than 4, which would not be possible without the hole. The collimating aperture effectively removes the high-emittance particles from the beam, thereby improving the transverse phase space quality. Decreasing the surface charge density at the cathode also enables the generation of a shorter electron beam.

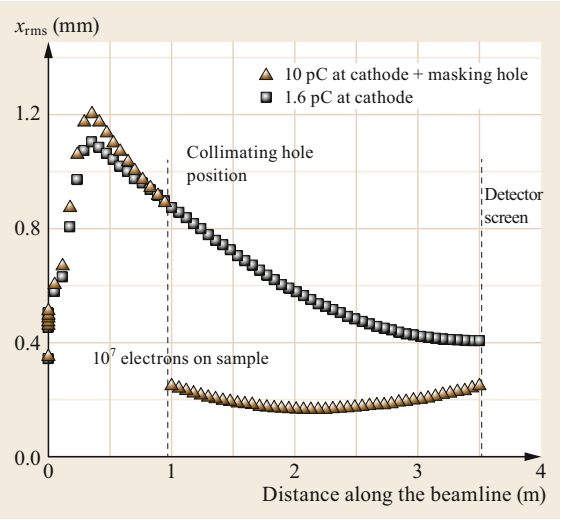

Fig. 19.11 General particle tracer (GPT) simulations of beam dynamics with and without collimating aperture

19.2.5 Detector

In conventional nonrelativistic UED, microchannel plates (MCP) are used to image keV electrons directly, amplifying the flux of low-energy electrons inside an image intensifier. The intensified electron flux is then converted by a scintillator to visible photons, which are subsequently fiber-optically coupled to a high efficiency charge-coupled device (CCD) camera. It is relatively straightforward to achieve single-electron detection capability due to the large gain of the MCP and the high light collection efficiency of the fiber-optics coupling.

MCPs have also been tested for MeV electrons, and high-quality single-shot diffraction patterns were obtained [19.93]. Blurring of the pattern was observed as a result of the large penetration depth of MeV electrons and the resulting excitation of secondary electrons in many surrounding microchannels. It was also found that, due to the active amplification process, the signal from the MCP had larger fluctuations, which might be a concern in single-shot measurements where very small changes in the pattern are to be detected. No performance degradation of the MCP or fiber optics was observed after long-term exposure to MeV electrons.

An effective alternative for the detection of MeV electrons is the use of optimized passive scintillator screens, which are low-cost and provide high electron-to-photon conversion efficiency and improved spatial resolution. A phosphor screen yields as many as a few thousand photons for each MeV electron due to the large penetration depth of MeV electrons. As an example, two recent papers reported calibration measurements showing greater than 10^3 photons per MeV electron from a Lanex Fine (a commercial version of phosphor P43) screen [19.94, 95]. In fact, considering an energy loss rate of 1.2–1.5 MeV cm^2/g for 1–4 MeV electrons and a screen density of 34 mg/cm^2, the total energy deposition by each electron is approximately $E_{loss} = 50$ keV. For an optimal choice of phosphor material and screen composition, the con-

version efficiency of this energy into output of visible photons is on the order of $\eta = 15–25\%$. Approximately half of these photons will exit from the screen side facing the CCD camera, while a roughly equal amount will exit from the back side. Since the photon spectrum is narrowly peaked at $h\nu = 2.27\,\mathrm{eV}$ (545 nm), we have $n_{\mathrm{scr}} = (1/2)E_{\mathrm{loss}}\eta/(h\nu) = 1.7–2.8\times10^3$ as an estimate of the number of photons emitted from each side of the screen per incident MeV electron. With a properly designed lens-coupling system with collection efficiency higher than 1% and a state-of-the-art CCD camera capable of single-photon detection, single-electron imaging is possible. This was demonstrated in the work of the UCLA group, where up to the ⟨800⟩ diffraction spot from a single-crystal 20 nm gold sample was detected in a single shot [19.96]. In order to further increase the photon yield per electron (enabling the use of less sensitive cameras), fluorescent screens with larger phosphor density or thickness (higher electron-to-photon conversion efficiency) and still reasonably small point spread function sizes, such as the Mitsubishi Chemical DRZ series standard screen, could be used.

Although it provides high sensitivity, this detection system suffers from several shortcomings. First, the P43 phosphor is subject to image burn-in. Intense fluorescence can persist at a low level for minutes afterward, even though the fluorescence $1/e$ lifetime is 0.7 ms. This is a distinct disadvantage when analyzing subtle differences in diffraction patterns. Faster phosphors are available, but they have reduced quantum efficiency and fluoresce at different wavelengths. Second, and more importantly, phosphor screens generally have a spatial resolution on the order of 50–100 μm. For the detector employed in the UCLA experiments, the size of the point spread function was around 64 μm. This comes from a combination of the minimum grain size and the film thickness. Ultimately, this limits the reciprocal space resolution of the system.

Further advances on the detector side are expected within the next few years. Outstanding issues include the spatial resolution and dynamic range of the detector. High spatial resolution can be achieved utilizing very thin scintillating screens and high-numerical-aperture optics to collect the light, but at the expense of detection efficiency. For example, the use of a 20 μm YAG:Ce crystal with an in-vacuum infinity-corrected microscope objective coupled to an in-air CCD recently demonstrated the potential for spatial resolution of features in the beam down to 3 μm [19.90]. Another possibility that has been studied in the framework of high-brightness beams for free-electron laser beamlines uses scintillating crystals observed in the Scheimpflug imaging condition to maximize the spatial resolution of the detector [19.97].

The other issue is related to the saturation of the diffraction pattern. When using an image intensifier, it is possible to set the electronic gain at a high level to achieve high detection efficiency, but it should be noted that with a camera well depth at a fixed value, the effective dynamic range is actually suppressed. To enable the detector to withstand the large intensity ratio between the direct beam and high-order spots, an effective solution is to coat a radially symmetric, variable neutral-density apodizing optical filter on the output side the phosphor screen. In principle, an extension of the dynamic range of over seven orders of magnitude is possible using this technique.

Another interesting development is the hybrid pixel array detector (EMPAD—electron microscope pixel array detector) developed at Cornell for scanning transmission electron microscopy [19.98]. The 128×128 pixel detector consists of a 500 μm-thick silicon diode array bump-bonded pixel-by-pixel to an application-specific integrated circuit. The in-pixel circuitry provides a 1000000 : 1 dynamic range within a single frame, enabling direct electron beam imaging while still maintaining single-electron sensitivity.

Finally, the introduction of direct electron detectors has played a critical role in the structural biology revolution of cryogenic electron microscopy [19.99]. Direct electron detectors are now expected to have a similarly dramatic impact on MeV electron diffraction microscopy. They hold the promise of very fast frame rates that will potentially enable spatial and temporal jitter correction, high spatial resolution (< 30 μm), and single-electron sensitivity [19.100]. Further work is needed to understand how to take advantage of the electron-counting mode in direct electron detectors for the high-brightness beams used in MeV UED.

19.2.6 Velocity Compression

For low beam charges, the 1.6-cell S-band photocathode RF gun alone can generate sub-50 fs rms electron pulses with adequate beam brightness to record single-shot diffraction patterns. However, breakthrough opportunities for new scientific discoveries can be enabled by crossing the 10 fs threshold in electron bunch length. For example, sub-10 fs electron beams are ultimately required to probe the fastest dynamics in solid-state systems and to directly observe bond-breaking in gas-phase molecular reactions [19.101–103].

Velocity bunching can be used to achieve very short bunch lengths. This technique makes it is possible to significantly compress the electron beam, reducing its bunch length by a large factor relative to the original laser pulse duration used in the photoemission process. In a velocity-bunching scheme, particles in the tail of

the beam are accelerated (typically via an RF cavity) more than the particles in the head, so that, following propagation in a dispersive beamline element (at energy of a few MeV, this is typically just a drift length), the particles arrive at a screen simultaneously (i. e., the bunch duration is compressed) [19.104, 105].

Velocity bunching was first implemented for UED using low-energy electron beams (keV) [19.36], but has also been shown at meter scales with electron beam energy of a few MeV [19.106]. To date, both nonrelativistic and relativistic velocity-bunching experiments have demonstrated well below 100 fs rms bunch lengths, but have not yet yielded bunch lengths measured in the single-digit-femtosecond range. One reason is that these extremely short bunch durations pose significant challenges in beam diagnostics [19.107].

Promising results have been reported recently for the generation of beams of both unprecedented bunch length (< 10 fs rms) and very low transverse emittance (≤ 20 nm), utilizing a compact beamline with an S-band RF gun and a bunching cavity [19.90]. Another important result of this work was the demonstration that a thick deflecting cavity could be used for the direct measurement of these beams due to a transverse kick cancellation effect which occurs when the beam undergoes a nonlaminar longitudinal focus inside the cavity. A cartoon illustrating the evolution of the pulse length in the UED beamline is shown in Fig. 19.12.

The shortest bunch length achievable is limited by longitudinal space charge repulsion as well as nonlinear longitudinal phase space (LPS) correlations induced by the sinusoidally varying field in the RF cavities. In practice, the RF curvature is typically the main limitation to the shortest bunch size achievable for velocity bunching with picosecond photocathode laser pulse duration. Various schemes have been proposed to mitigate the RF curvature effects, such as the use of a harmonic linearizer [19.108] or a debunching phase in the gun to stretch the scale of the nonlinear distortions, allowing them to be linearized in the bunching cavity [19.109].

In the experiment, an ultrashort (sub-100 fs) laser pulse was employed on the cathode to generate a small longitudinal emittance and reduce the head–tail differences in the RF wave seen by the bunch. Figure 19.12 compares the longitudinal and transverse dynamics with a 1 ps and 100 fs rms laser pulse length, simulated with the space charge code general particle tracer [19.110], and shows how, with no linearization scheme applied, the shorter laser pulse allows a smaller longitudinal focus (down to 6 fs) to be achieved.

The combined action of the RF-induced energy chirp and the longitudinal space charge (LSC) effects determine the dynamics of the longitudinal compression and the location of the shortest pulse length. Because of the transverse dependence of the LSC force, different radial positions in the beam arrive at the optimal longitudinal compression at different times. A collimation hole can be used to select the core region of the beam where the compression dynamics is more homogeneous.

We conclude this section by quantifying the possible role of the longitudinal pulse profile in resolving a structural change of a given decay time or oscillation period. This is an important point, as different communities use different parameters to characterize bunch length, such as rms or full width at half maximum (FWHM). For well-defined longitudinal beam shapes, e. g., rectangular or Gaussian distributions, the rms and FWHM values differ only by a fixed shape-dependent constant, but as a result of compression schemes, longitudinal beam profiles become more complicated. In many cases they are characterized by sharp spikes and long tails, especially when a relatively long pulse is compressed and the final compression is dominated by the RF curvature. It then becomes important to understand how to quantify the temporal resolution. In electron diffraction, each electron in the beam will contribute to the signal on the detection screen. The situation is different, for example, if the ultrashort compressed beams are used to drive free-electron laser

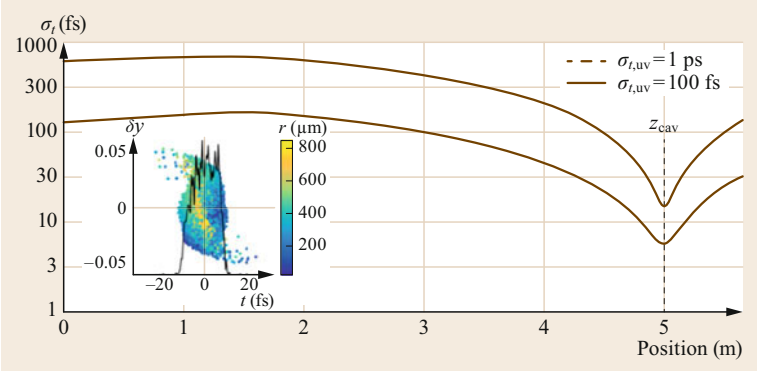

Fig. 19.12 Bunch length versus position along beamline for two different initial pulse lengths. At the compression point, the minimum bunch length can be well below 10 fs. Reprinted with permission from [19.90]. Copyright 2016 by the American Physical Society

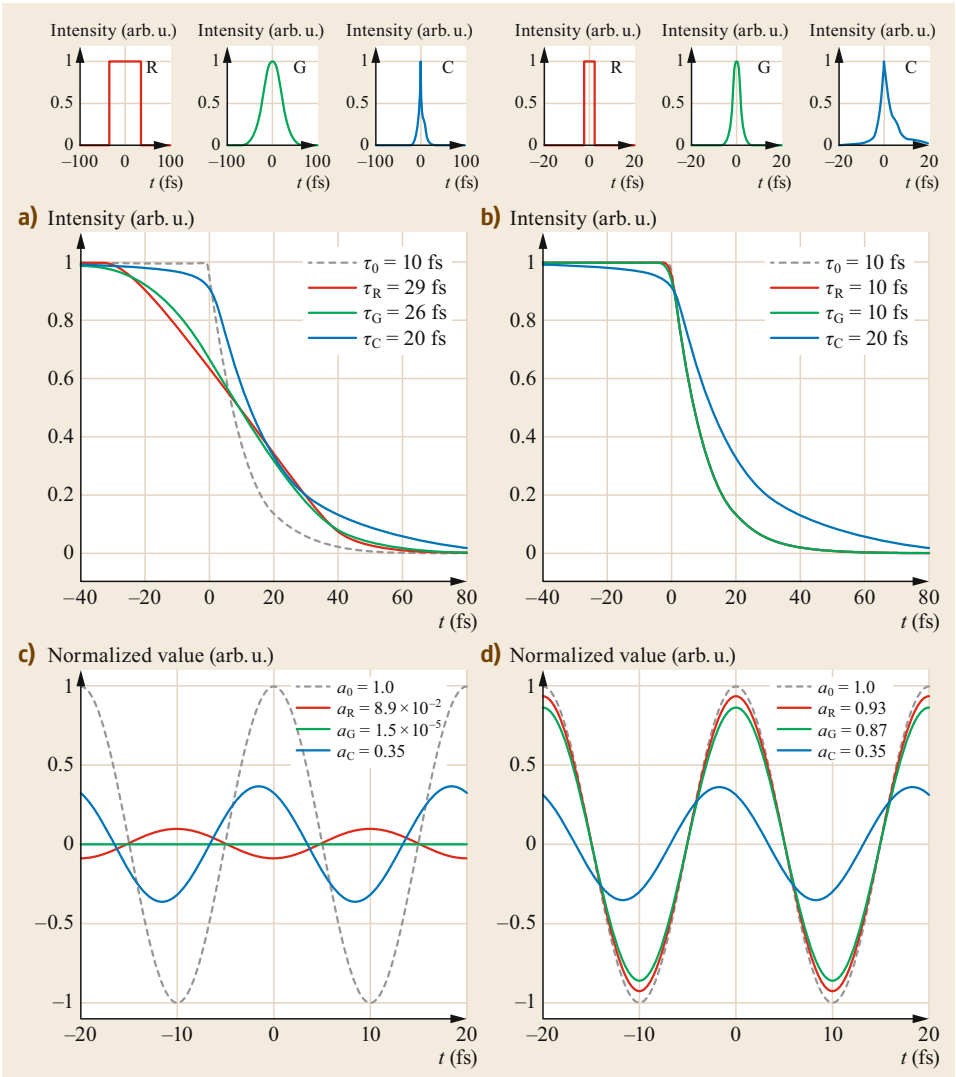

Fig. 19.13a–d Pulses with longitudinally rectangular (R, *red*), Gaussian (G, *green*), and complex shapes (C, *blue*, see text for details) are used to measure **(a,b)** an exponential decay and **(c,d)** an oscillating structural change. In **(a,c)** the three pulse have the same rms widths of 20 fs, and in **(b,d)** the pulses have equal FWHM widths of 4 fs

amplifiers. In this case, the instability amplification process selects the brightest part of the beam (the spike in beam current) and greatly enhances the contrast with the low-current portions of the beam.

In Fig. 19.13, we compare a Gaussian-like pulse shape (denoted by G) with different shapes characterized by the same rms or FWHM bunch length. An interesting case to consider is a pulse shape (denoted by C) where 80% of the electrons are bunched into a 4 fs FWHM peak, but the remaining 20% extend in a long tail trailing the beam, so that the rms width of the entire pulse is 20 fs. This mimics the typical case where the RF-induced nonlinearities dominate the final bunch length. Deconvolution techniques may be used to retrieve the intrinsic time constant from the measurement results if the longitudinal beam profile can be mapped with high precision.

19.2.7 Bunch Length Diagnostics and Streaking

MeV UED sources are approaching temporal resolution in the few-fs regime. Diagnostics such as very high-voltage (> 500 kV) deflecting cavities may be employed for this bunch length range, but considering the relatively large deflection momentum applied to the beam, a thorough analysis of inherent cavity vertical defocusing, intracavity bunch lengthening due to the applied energy spread, and higher-order nonlinearities must be performed to ensure measurement validity [19.92]. Laser-triggered deflectors were developed by *Kassier* et al. [19.111] and have been employed for both time-stamping and streaking diagnostics to measure bunch lengths. Deflecting structures that use high frequencies, such as conventional X-band (and

higher-frequency) cavities, as well as deflecting structures based on terahertz [19.112] and optical (laser-driven [19.11]) or plasma-based [19.107] diagnostics, should be considered, due to the linear scaling of the streaking power with the field frequency.

Questions have been posed as to the suitability of deflecting cavities to measure bunch length for velocity-compressed beams in cases where the bunch length would vary significantly within the cavity [19.106]. However, at beam energies of a few MeV and when the transverse dimensions are much larger than the longitudinal dimensions, the longitudinal focus is typically a crossover waist, even with the inclusion of space charge forces. That is, as the beam comes to a longitudinal focus, particles in the tail end up at the head of the beam, and vice versa [19.92]. By placing the longitudinal focus position at the center of the deflecting cavity, it is possible to take advantage of this nonlaminar motion to obtain a cancellation in the integrated transverse momentum kicks from the streaking cavity.

This can be seen directly using a simplified model of the interaction with the streaking fields. A particle with a trajectory $z = c\beta t + z_0$ will accumulate an integrated momentum kick of

$$\Delta p_y = \frac{F_0}{c\beta}\int_{-L/2}^{L/2} \sin\left(\frac{\omega(z-z_0)}{c\beta}\right) \mathrm{d}z$$
$$= -\frac{F_0}{\omega}\sin\left(\frac{L\omega}{2c\beta}\right)\sin\left(\frac{\omega z_0}{c\beta}\right), \qquad (19.9)$$

where F_0 is the streaking force amplitude and L is the cavity length. Note that the position is measured from the center of the cavity, and the phase of the RF wave is chosen such that a reference particle at $z_0 = 0$ experiences no deflection. In the absence of other effects, the only residual induced angular kick is proportional to the temporal beam duration at the center of the cavity regardless of the bunch length at the cavity entrance and exit. Using this method, it is possible to retrieve the bunch length by a detailed comparison of the deflector-on/deflector-off shots. Assuming Gaussian beam distributions with rms width σ, the measured bunch length is then

$$\sigma_t = \frac{mc^2\beta\gamma}{\omega e V_\mathrm{d} L}\sqrt{\sigma_{\mathrm{y,on}}^2 - \sigma_{\mathrm{y,off}}^2}\,,$$

where V_d is the effective deflector voltage, ω is the deflector angular frequency, L is the drift length between cavity and observation screen, and $mc\beta\gamma$ is the average beam momentum.

The introduction of deflecting cavities in electron beamlines has also led to renewed interest in a different scheme for time-resolved electron diffraction. Even in the early days of UED, researchers recognized the possibility for an alternative setup in which the diffracted electron beam is streaked using deflecting plates to record the time evolution of the changing pattern [19.16] (Fig. 19.14). The advantage in such a configuration is that a short electron bunch is no longer required, and the temporal resolution is determined by the sweeping speed of the plates or, more generally, by the resolution of the streak camera system. The large (a few ps) jitter in the photoconductive switch providing the synchronization between the beam and deflecting voltage, and the slow sweeping speed that can be achieved have made this approach less favorable than the more conventional pump-and-probe scheme characterized by time-delay scans. *Baum* and *Zewail* [19.113] proposed an alternative method to bypass the streaking plates. It takes advantage of the strong chirp (time–energy correlation) that electron pulses naturally develop in the propagation from the cathode due to the space charge forces. In this promising scheme, which is currently awaiting an experimental demonstration, an energy-filtering device (a spectrometer) is used to effectively analyze in time the diffraction signal taking the role of the streaking plates [19.114, 115].

Using an RF resonant cavity for the deflection enables higher deflecting voltages, which together with a relatively high oscillation frequency offers faster sweeping speeds than those possible with traditional sweeping plates [19.114, 116]. The other key ingredient of the technique is the use of intense relativistic electron beams. The peak current in a 4 MeV electron beam from an RF photoinjector can be in the range of tens of amps. With 10^7–10^8 particles per pulse in a 15–20 ps-long electron beam, it in fact becomes possible to acquire the entire time-history of the ultrafast process within a single pump-and-probe event. Using such beams in conjunction with an RF deflector eliminates the need for time-delay scanning and offers the possibility for truly single-shot studies of irreversible processes in ultrafast structural dynamics.

The reconstruction of the entire time-history of an ultrafast structural process using a single continuously time-resolved diffraction pattern has been demonstrated. The test process we study is the ultrafast laser-induced heating and melting of a single-crystal 20 nm-thick Au foil.

19.2.8 Time-Stamping

Obtaining the shortest possible electron bunch length has undoubtedly been a major effort in the development of MeV UED. Nevertheless, as seen in (19.6), the temporal resolution of the femtosecond relativistic electron

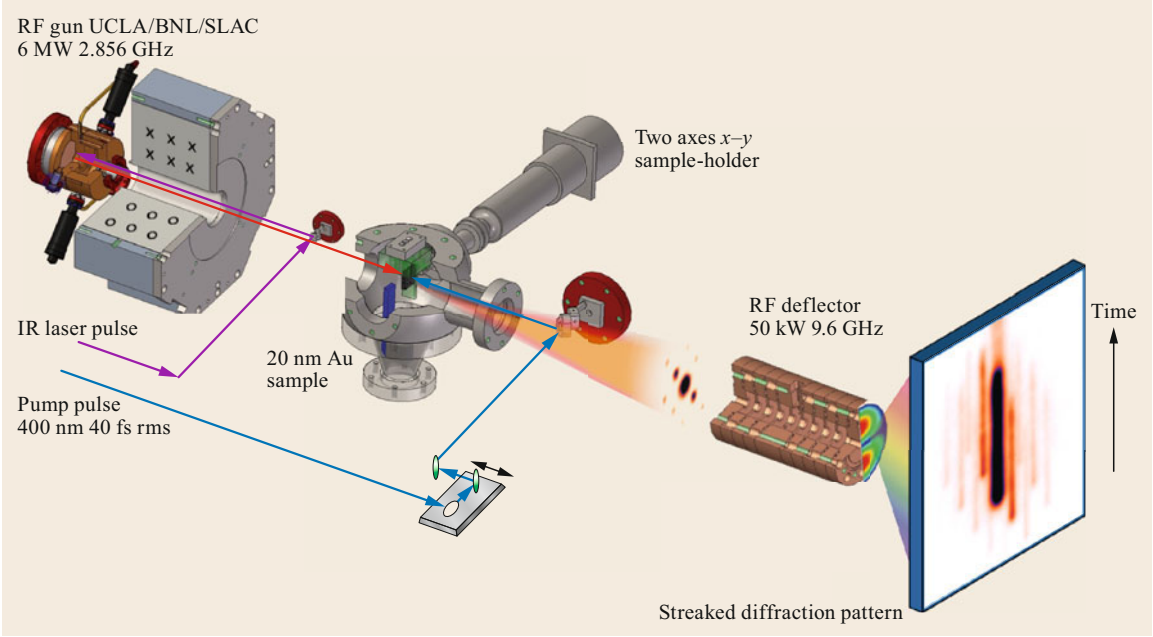

Fig. 19.14 Continuously time-resolved UED

diffraction (FRED) technique varies. In particular, the uncertainty in the relative time of arrival between the pump and the probe beam constitutes a major concern when bunch lengths fall below 100 fs.

In a typical (pump–probe) UED study, the optical pump triggers a dynamic process, and the electron probe is used to measure the instantaneous atomic structure. The dynamics can be resolved by adjusting the delay between the pump and probe. The temporal resolution of a pump–probe study is bounded by the finite temporal durations of the pump and probe pulses, but it is further limited by the ability to precisely control the pump–probe delay. Often, the shot-to-shot relative time-of-arrival (ToA) jitter between the pump and probe pulses is larger than their pulse durations, and thus a precise timing diagnostic is needed to measure their relative delay at ultrashort timescales. Such a measurement can be used to quantify the fluctuations and to characterize the temporal resolution of the technique, but if it can be obtained in a single shot, it can also be used to re-sort the time-series data and improve the temporal resolution (time-stamping).

Ultrafast electron scattering applications, laser accelerators, inverse Compton scattering sources, and more generally any scheme requiring synchronization between a laser and an electron beam all share the common issue of controlling the relative ToA jitter between the electron beam and the laser. ToA diagnostics have been developed in the context of pump–probe experiments in the areas of both x-ray FEL [19.117, 118] and advanced accelerators [19.119, 120], and for ultrafast electron diffraction (UED) [19.121].

Measurement schemes typically rely on measuring a reference optical or RF signal (referred to in this work as the diagnostic laser) after an indirect interaction with the probe. For instance, sub-10 fs accuracy has been demonstrated using the modulation of an RF signal in electro-optic modulator (EOM) pickups [19.122]. Alternatively, a diagnostic laser can be used to imprint an energy modulation on a chirped beam in an undulator to determine the temporal structure of the pump and probe [19.119]. The cross-correlation of the diagnostic laser and the edge radiation from an undulator has been used to achieve 5 fs resolution [19.118]. More recently, *Harmand* [19.123] and then *Hartman* [19.117] introduced a timing diagnostic for pump–probe experiments at LCLS based on free carrier density-controlled transmission of an 800 nm laser through a silicon nitride membrane, achieving sub-fs resolution.

For RF-based particle accelerators, the jitter on the pump–probe time of arrival is related to the phase and amplitude jitter introduced in the RF amplification chain. For RF photoinjectors, the synchronization accuracy between the laser and radio-frequency low-level oscillators adds an important contribution to the total jitter, typically on the order of a few tenths of a degree of RF frequency. For low-energy beams, RF amplitude (and therefore beam energy) fluctuations contribute significantly to the arrival time of the electron beam relative to an external laser pulse at a fixed

location along the beamline. The combination of these effects limits the temporal resolution of pump–probe techniques to 50 fs when using an S-band RF photoinjector. A possible solution for increasing the temporal resolution in ultrafast dynamics studies is to time-stamp each shot and then perform an offline temporal rearrangement of the data. A similar setup was proposed and successfully tested at the short-pulse photon source beamline at SLAC [19.124], where a one-to-one correlation was obtained between the electro-optic sampling (EOS) time-of-arrival stamp and the evolution of an ultrafast phase transformation (the nonthermal melting of an InSb crystal).

There are many time-stamping techniques that can be used to retrieve laser and electron beam relative time-of-arrival information. In general, one relies on a prompt interaction where either the laser induces an observable change on the electron beam, or vice versa. The actual implementation is dependent on the wavelength of the laser and the energy of the electron beam. Ponderomotive scattering [19.125], laser-triggered deflecting plates [19.126], and terahertz-based streaking [19.112] are some of the possibilities for electron beam deflection using a laser. The inherent advantage in all of these techniques is that they are feasible with very low beam charge, since the only requirement for the beam is that it is detectable. The drawback, however, is that because the electron beam trajectory is affected by the interaction, the technique must be used on the undiffracted core of the beam, or the entire diffraction pattern is shifted.

Nondestructive diagnostics uses only the fields of the beam to induce a change, such as on the reflection or transmission of a laser pulse, and can also measure the relative time-of-arrival delay with good accuracy. The drawback is that the minimum field level that can be detected is usually in the range of a few MV/m, thus requiring a relatively large (100 fC or larger) beam charge.

The noncollinear 90° crossing EOS geometry has been used to spatially encode the signal from the electron beam onto the transverse profile of a laser pulse [19.121] (Fig. 19.15). The ZnTe electro-optic crystal is not required to intercept the beam, so this scheme can be used for nondestructive diagnostics. Accurate timing determination with sub-50 fs temporal resolution has been demonstrated in a single shot from a < 1 pC beam charge. A fast algorithm processes the images and extracts a number for each beam shot, which is used to time-stamp the diffraction patterns. A postmortem sorting algorithm then reorganizes the images to allow beating of the jitter temporal resolution. The limitation with this approach arises from the fact that a minimum charge of 1 pC is required to nondestructively extract a timing signal from the relativistic beam. This could be improved in multiple ways. For example, using the main undiffracted beam after the interaction, destructive diagnostics could be used. The use of different electro-optic crystals with larger nonlinear coefficients could also improve the signal-to-noise ratio of the technique.

A different ToA measurement scheme based on gating the transmission of long-wavelength radiation through a small slab of semiconductor (germanium) by a very low-charge (sub-pC) electron beam has also been demonstrated [19.127]. This scheme has unique characteristics. First, the technique is designed for use in time-resolved studies where the pump laser is tuned in the mid-infrared region of the electromagnetic spectrum. The use of long-wavelength lasers is often invoked in order to direct pump lattice excitations. For example, free-carrier dynamics in semiconductors has been studied extensively using terahertz-pump/terahertz-probe spectroscopy [19.128, 129]. Second, the scheme is designed to yield ToA information even with the use of very low beam charges compatible with MeV UED beamlines, which often use less than 100 fC charge per bunch [19.5]. This fills an important gap in the use of these machines, as other ToA measurement schemes [19.122] are limited to charges greater than a few pC.

In order to time-stamp ultralow beam charges, the semiconductor gating technique used by *Harmand* at LCLS [19.123] was adapted to an existing radio-frequency (RF) photoinjector-based UED setup [19.73]. The main difference is in the choice of semiconductor in order to take advantage of favorable scaling of the effect at lower laser frequencies. A smaller density of free carriers is needed to obtain a measurable signal when using long-wavelength lasers. Furthermore, since electrons deposit their energy more effectively than x-rays when passing through matter, a lower flux is required to generate appreciable free-carrier density in the semiconductor material. While LCLS has 10^{12} photons per pulse, acquisition of a timing signal with 10^6 electrons per pulse has been demonstrated. It should be noted that passing the electron beam through the germanium destroys the beam. It would thus be necessary to use the undiffracted core of the beam (which is usually passed through a hole in the UED detector) to implement this method as a ToA time-stamping diagnostic.

19.2.9 Start-to-End Simulations

Computational modeling is central to the development of MeV UED, and the electron source community has capitalized on the recent advances in computational tools such as multi-objective optimization, three-dimensional (3-D) electromagnetic solvers, and point-to-point space charge algorithms.

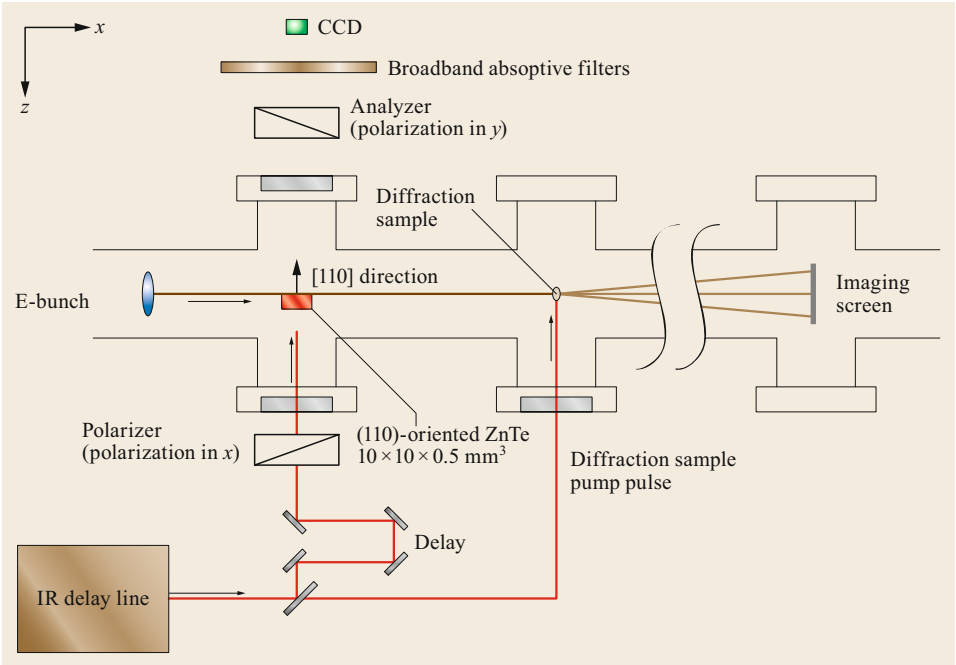

Fig. 19.15 Scheme for nondestructive single-shot time-of-arrival determination. A clear signal was obtained using a less than 1 pC beam charge in the main beam. After [19.121]

Smooth potential-field models (with frame-of-reference slices) are sufficiently accurate for modeling beams with emittance and energy spread levels we are currently concerned with. The next step will be to simulate individual electron–electron interactions. Coulomb scattering (intrabeam scattering) can be included in 3-D accelerator simulations with two-particle pair statistics or heroic point-to-point simulations. For very cold beams, the random spacing of electrons leads to induced thermal motion, similar to nonlinear free energy [19.130] on a microscopic level, and thus simulations need to include point-by-point models of this disorder-induced heating. Fast pairwise algorithms may be able to reduce the computational time to order $N \log N$ for N electrons [19.86].

For optimization of the diffraction patterns and the temporal resolution of the technique, particle-tracking codes such as GPT, IMPACT-T, or ASTRA are typically used starting from the cathode. The interaction with the sample is modeled after applying the kinematic diffraction approximation using an external code that acts on the phase space from the particle-tracking simulation, which is resumed immediately after the sample to propagate the particles up to the detector plane.

Particle-tracking code modules are available for calculating the scattering probabilities of few-MeV electrons in a thin sample foil and applying the angular kicks to the particle distribution. Only a few metal choices and a limited number of diffraction orders have been implemented at this time. Nevertheless, it is important to be able to run a fully consistent start-to-end model of the experiment. For example, GPT can follow the particles in three dimensions and has a powerful algorithm for space charge field calculations. This simulation can be very useful for studying the influence of space charge effects on spatial resolution. It has been shown that if the nondiffracted beam remains intense, the radius of the diffraction rings is perturbed due to space charge repulsion, and a systematic correction needs to be applied.

Multi-objective genetic algorithms (MOGA) have been proven very useful in the optimization of beamline parameters for a variety of applications [19.66], and have also recently been applied to high-energy electron diffraction [19.131]. Finally, the inclusion of photoemission physics is another area where novel computational methods are expected to enable rapid progress in obtaining even more accurate models of MeV UED performance [19.132].

19.3 Applications

The past decade has witnessed tremendous progress in key technologies for MeV UED. It is now feasible to construct a complete MeV UED system to generate high-quality data and bring new insight into many scientific areas. In this section we will briefly review the most recent scientific results with MeV UED.

Aside from the potential for improved spatial and temporal resolution in MeV UED, there are at least two main areas where pulsed, high-gradient relativistic sources have unique advantages over conventional UED techniques. They are (i) high-pump-fluence experiments, where the repetition rate is limited either by damage or by laser-induced heating, and (ii) gas-phase experiments, where velocity mismatch typically limits the probed volume [19.133].

19.3.1 Solid-State Systems

MeV UED is ideally suited for solid-state sample experiments that require a high level of pump excitation, in which the repetition rate of the pump may be limited to well below 1 kHz to avoid laser heating-induced sample damage. In extreme cases, the pump fluence can be so high that the sample is damaged with every shot, and the repetition rate is limited by how fast one can mechanically move to a fresh spot on the sample, which can be as slow as 1 Hz. For these measurements, it is naturally desirable to keep the number of electrons per pulse as large as possible for a given temporal resolution, probe size, and reciprocal space resolution, which thus demands the highest possible beam brightness.

The first demonstration of MeV UED using a beam from an RF photoinjector was the study of irreversible structural dynamics in a solid-state crystal with sub-ps temporal resolution. The test process involved the laser-induced melting of a single-crystal 20 nm-thick gold sample. Single-shot diffraction patterns are shown in Fig. 19.16. It is worth noting that each diffraction pattern was obtained using a single sub-200 fs electron bunch.

For each diffraction spot, a two dimensional Gaussian fit can be used to calculate its amplitude, the center position, and the width. The variation in the normalized amplitude for each Bragg peak can be estimated as $\approx 1\%$ looking at the stability of the trace in Fig. 19.16

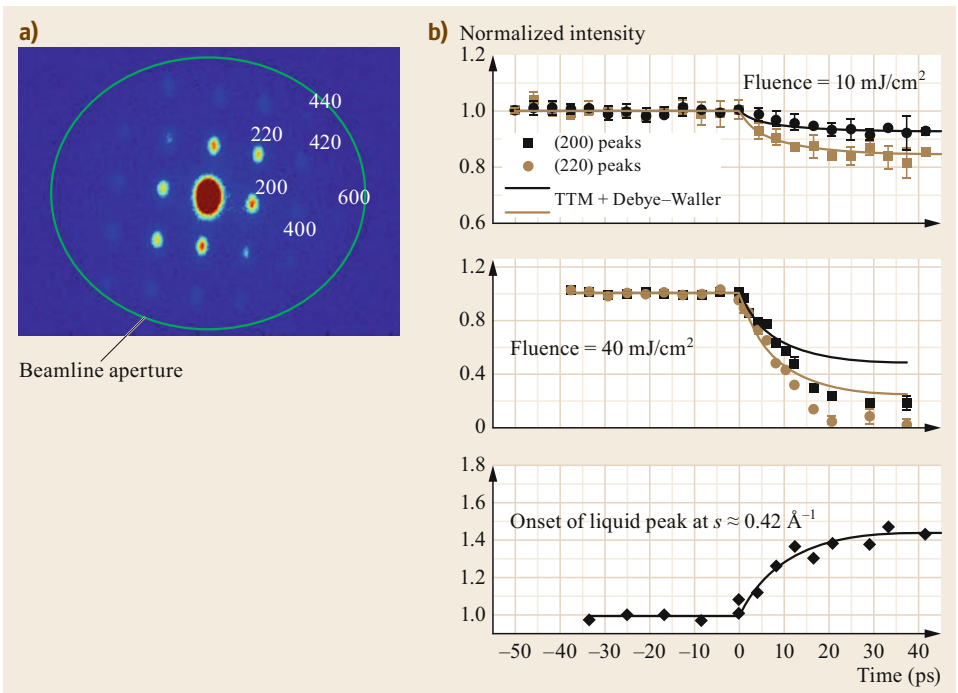

Fig. 19.16a,b Laser-induced heating and melting of a single-crystal gold sample studied using single-shot MeV electron diffraction patterns [19.45]. **(a)** Single-shot diffraction pattern from a single-crystal gold sample. **(b)** Evolution of Bragg peaks for low and high fluence as a function of time. Each point is recorded after moving the pump–probe delay line stage. Reprinted from [19.45], with the permission of AIP Publishing

for the time delays when the laser arrives after the electron beam.

The observed behavior of the Bragg peak amplitudes provides a direct test of our understanding of the laser-induced heating and melting processes in a metallic single-crystal sample. The laser energy is absorbed within an optical skin depth (7–8 nm), creating a population of fast electrons that move ballistically across the sample at Fermi velocities [19.134]. Because of the strong electron–electron scattering, the electron distribution thermalizes quickly, so that shortly (< 100 fs) after illumination, it is possible to define a homogeneous electron temperature across the sample. At this point, with a timescale controlled by the electron–phonon coupling constant, diffusive heat transfer to the lattice subsystem takes place, leading to electron and lattice temperature equilibration. Ballistic electron transport modifies the depth over which the laser pump pulse deposits its energy. This contribution is important and can be included by modifying the penetration depth of the laser energy term when treating the problem with a two-temperature model (TTM) [19.135].

The increase in lattice temperature is the origin of the loss of coherence of the Bragg peaks. The thermal random motion induced by the electron–phonon coupling acts to blur the atomic positions in the crystal and decreases the Bragg peak amplitudes (Debye–Waller effect). The predictions for the variation in the Bragg peak amplitudes obtained using a TTM for the Au lattice are shown in Fig. 19.16. The model fits the data well when the electron–phonon coupling constant—an important parameter for strongly correlated electron systems—is $\lambda = 0.15$, in excellent agreement with the value reported in the literature [19.136]. The data also show that higher diffraction orders disappear faster than lower ones, consistent with the scattering vector dependence in the Debye–Waller factor.

When the fluence is raised to $35\,\mathrm{mJ/cm^2}$, the lattice temperature rises above the melting point; the solid becomes superheated at first, and then the phase transition takes place. This can be observed by the departure from the Debye–Waller factor TTM scaling in the peak amplitudes between 12 and 18 ps from the time when the laser hits the sample. During the same time interval, by integrating the diffraction pattern over regions where the signal is not shadowed by diffraction spots, and again comparing with the results from the laser-off images, it is possible to observe the rise of the liquid correlation function peak at around $0.42\,\mathrm{Å}^{-1}$.

Similar pump–probe MeV UED measurements of gold nanofilms in the strong-pump irreversible-melting regime were carried out at Osaka University [19.137, 138]. More recently, researchers at SLAC succeeded in measuring the structural dynamics of gold nanofoils in the warm-dense-matter regime, revealing the underlying melting mechanism in the homogeneous and heterogeneous regimes [19.139]. To achieve the required laser fluence (up to $90\,\mathrm{mJ/m^2}$ at 400 nm) with available total laser energy, the pump spot size, and hence the probe size of the electron beams, had to be reduced to $120\,\mu\mathrm{m}$ FWHM, which posed a significant challenge for the generation and control of electron beams to deliver the required pulse duration and reciprocal space resolution.

Another advantage of MeV versus keV electrons is the smaller elastic cross section, which makes them well suited for studying relatively thick samples with minimal multiple scattering. This is important when trying to match the pump and probe volume, depending on the optical response of the material (i. e., the absorption length). This is also a critical advantage and enables measurement of diffuse scattering from nanofilm samples. In a recent experiment, MeV electron beams were used to track the diffuse scattering signal for laser-excited single-crystal gold nanofilms [19.140]. The sample thickness was 20 nm, or about the elastic scattering mean free path of MeV electrons for gold; thus the diffraction signal was dominated by single scattering events. The diffuse scattering signal can be found around the main Bragg spots. By tracking the temporal evolution of the diffuse signal, one gains insight into how laser-heated electrons transfer energy to certain phonon modes along different directions in the Brillouin zone.

In another successful experiment with MeV UED, the sample was a monolayer MoS_2, and for the first time the ultrafast structural dynamics of two-dimensional (2-D) materials was studied directly [19.141]. By recording the changes in the intensity, position, and width of the diffraction spots after laser excitation, the in-plane displacement and electron–phonon coupling and rippling of the monolayer were observed. From a technical point of view, this experiment demonstrates that although MeV electrons have a smaller elastic cross section than lower-energy electrons, they are still capable of providing high signal-to-noise ratio diffraction patterns for even the thinnest samples. The ratio between the elastic cross section, which yields the diffraction signal, and inelastic scattering, which causes radiation damage, is roughly the same for electrons of a few MeV to hundreds of keV. In this experiment, no electron beam-induced radiation damage was observed, because of the very low dose employed.

There are several other reported pump–probe experiments performed with MeV UED [19.142–144].

19.3.2 Gas-Phase Systems

Historically, electron beams have been the preferred choice over x-rays for studying molecular structures in gas-phase systems [19.145] where the column density of the sample is extremely low. To determine molecular structures with adequate spatial accuracy, the wavelength of the probe should be ≈ 1 Å or shorter. At these wavelengths, the scattering cross section of electrons is five to six orders of magnitude larger than that of hard x-ray photons. From an instrumentation point of view, a complete electron diffraction apparatus, including electron beam generation, control, and detection, as well as gas-phase sample delivery subsystems, is compact enough to fit into a typical university-scale lab. The relatively low cost, compactness, and flexibility of these systems provide a tremendous opportunity for precise structural measurement and instrumentation development.

Time-resolved gas-phase electron diffraction (TR-GED) combines the traditional gas-phase electron diffraction (GED) with femtosecond lasers, which are used for both exciting the gas molecules and generating electron beams. TR-GED thus possesses great potential to eventually enable direct mapping of structural dynamics at atomic length and timescales. It complements photon-based spectroscopy (femtochemistry), which tracks the electronic dynamics, to provide a complete picture of the dynamics of molecules after laser excitation.

TR-GED was pioneered in the early 1990s by Prof. *Zewail* and his group at Caltech [19.29, 146–149]. The early instruments were based on keV electron guns and beams, and achieved tens of picoseconds to picosecond temporal resolution. The temporal resolution was limited by two main factors. First, strong space charge effects lengthen the duration of an electron beam, and this effect increases as the number of electrons per pulse or charge density increases. Typical pulse durations are ps or longer, with only a few thousand electrons per pulse. The second issue was the so-called *velocity mismatch* problem. The velocity of keV electrons is a small fraction of the speed of light c, while the pump laser pulses travel at c. Thus, for an extended sample volume (usually a few hundred micrometers in both thickness and lateral size), different regions of the sample can experience different pump–probe delay, and the temporal resolution is limited at the ps level. As discussed earlier in this chapter, RF compression can be used to reduce the pulse duration to a few hundred fs for 10^6 electrons per pulse. There have also been efforts to tune the angle of incidence as well as the pulse-front tilt of the pump laser relative to the probe electron beams to eliminate the velocity mismatch term. Still, the best temporal resolution demonstrated for TR-GED with keV electron beams is at the ≈ 1 ps level.

An alternative and more direct approach for tackling these challenges is the use of MeV energy electrons. Higher beam energy can very effectively suppress the effects of longitudinal space charge forces which cause bunch lengthening. By also applying the RF compression technique to MeV electron beams, one can generate 10 fs or shorter beams suitable for TR-GED, while the contribution from the velocity mismatch can be easily maintained at a negligible level. For example, 4 eV kinetic energy electrons travel at $0.994c$. With a pump laser at 50 mrad with respect to the electron beam and 200 µm-thick gas volume, the velocity mismatch is less than 4 fs. Thus the use of MeV TR-GED holds great promise for reaching temporal resolution of sub-100 fs—potentially even 10 fs—to track some of the fast molecular dynamics during photochemical reactions.

The first TR-GED experiments with MeV electrons were recently successfully conducted at the SLAC National Accelerator Laboratory [19.150, 151]. The design and operation of the machine has been reported in detail elsewhere [19.152, 153]. A 3 GHz radio-frequency photocathode gun generated 3.7 MeV electron beams. Typical bunch charge was 6 fC or 4×10^4 electrons per pulse that scattered from gas molecules. No RF bunch compressor was available in the initial experiments, and the RF compression of the gun itself [19.154] was used to generate short, sub-100 fs rms pulse durations. The very first physical phenomena measured by TR-GED were the rotational wave-packet dynamics of nonadiabatically laser-aligned nitrogen molecules [19.150]. The electron beams and instrument provided sub-Å spatial and 100 fs rms temporal resolving power to track the rotation of N_2 molecules following excitation by linearly polarized laser pulses. In another experiment, MeV TR-GED was used to directly image vibrational wave-packet dynamics in laser-excited I_2 molecules. The measurement results visualize how the interatomic distance, i. e., the bond length, of I_2 oscillates from 2.7 Å in the ground state to 4 Å in the excited B state with a 400 fs period following laser excitation.

Future directions of instrumentation development for GED include (i) further improvement in temporal resolution to the 10 fs level, and (ii) increasing the signal-to-noise ratio of diffraction patterns by both higher bunch charge and higher repetition rate.

19.4 Future Developments and Outlook

19.4.1 Time-Resolved Electron Microscopy

An ambitious goal of the community is to push the limits of current UED technology and take advantage of the high brightness of the intense MeV electron beam for imaging applications. A current trend in transmission electron microscopy is to add the temporal dimension to the instrument capabilities, thus enabling real-time observation of microscopic dynamic processes.

One of the first successful attempts at developing high-speed transmission electron microscopy (TEM) at TU Berlin produced an instrument capable of taking 10 ns temporal snapshots of the samples with spatial resolution of a few hundred nm [19.155, 156]. More recently, dynamic transmission electron microscopy (DTEM) at LLNL [19.157, 158] demonstrated single-shot images of samples with 10 ns temporal resolution and 10 nm spatial resolution. At the relatively low energy (200 keV) of this instrument, electron–electron (e–e) interactions within the beam in the lens crossovers prevent the use of a beam current higher than a few mA and limit the spatiotemporal resolution. The ultrafast electron microscopy (UEM) technique developed at Caltech employs a different scheme—the stroboscopic method—using on average one electron per pulse to record images of reversible dynamic processes with ≈ 500 fs temporal resolution [19.159]. Because single-electron packets have no space charge broadening, the problem is eliminated at its roots, and the spatial resolution can approach a level similar to that achieved in conventional TEM. On the other hand, millions or more electron pulses are needed to record each image, with the repetition rate typically limited to the MHz range to allow enough time for the sample to relax to its initial state. With this technique, one is restricted to dynamic processes occurring exactly the same way for each pump–probe cycle.

Another possible solution is to increase the energy of the beam to the MeV level to take advantage of the relativistic suppression of the space charge forces and capture a TEM image in a single shot (Fig. 19.17). There are two major limitations to expanding the capabilities of the MeV diffraction camera toward high-spatial-resolution imaging mode: (i) the limited beam coherence from the photocathode in the RF gun, and (ii) the technical difficulties associated with building strong lenses for relativistic energy beams.

It is important to understand the different requirements for single-shot imaging relative to conventional TEM and relativistic UED. Applying the Rose criterion [19.160] to evaluate the minimum number of particles needed to generate a clear signal above the noise induced by the Poisson statistics, we find that 100 or more electrons are needed per spatial resolution unit d to maintain the shot-noise below 10% and achieve a signal-to-noise ratio of 5 (assuming 50% contrast). Therefore, roughly 4×10^6 electrons (0.6 pC) are required to form an image with 4×10^4 resolution units with an area of $200d\times200d$. If we want to pack this number of electrons into a single pulse with 10 ps bunch length, the peak current in the microscope column will be 60 mA or larger.

For these large peak currents, several orders of magnitude higher than those in conventional TEM and 10−100 times larger than in DTEM, there are a number of reasons to increase the electron energy to the MeV level.

First, the higher electron energy significantly alleviates issues related to stochastic Coulomb scattering, especially in the crossover regions after lenses where the beam density is the largest and e–e scattering causes loss of coherence and increased phase space area. This effect cannot be compensated for by simply increasing the strength of the lenses, since random collisions essentially heat up the phase space. The effect of charged particle collisions in a crossover was studied analytically by *Jansen* [19.62] and numerically by *Reed* et al. [19.161]. More recently, *Li* and *Musumeci* analyzed an MeV TEM column using a point-to-point model for e–e interactions, and found the blur on the final image to be the major limiting factor to achieving spatial resolution below 10 nm for 5 MeV electrons [19.108].

Second, relativistic electron sources are typically characterized by very high extraction fields at the cathode, compared to conventional TEM, which is limited by arcing in the gun to gradients smaller than 10 MV/m. The higher electric fields at the cathode enable (for a given beam charge) decreased source size and improved beam brightness. Recent analysis shows that for an initial cigar aspect ratio (long and narrow pulse), a relatively large charge can be extracted from a small transverse region of the cathode. For example, a charge greater than 1 pC could be extracted from a 10 μm spot size with a bunch length of 10 ps in the 100 MV/m peak field of an S-band photocathode RF gun [19.65]. Another possibility discussed in [19.162] would be the use of a large-area hollow cone photocathode to generate the illumination probe beam, reducing the space charge effects associated with the small source for full-field time-resolved TEM.

Apart from the challenging demands for the beam flux, small transverse emittance and very low energy spread are also critical to minimizing the effects of

spherical and chromatic aberrations to reach spatial resolution at the 10 nm level. For incoherent imaging, we can obtain simple estimates for acceptable beam parameters, knowing the spherical and chromatic aberration coefficients (C_s and C_c, respectively), in order to obtain 10 nm spatial resolution yielding a relative energy spread lower than 10^{-4} and a collection semi-angle of $\lesssim 5$ mrad.

Combined with the Rose criterion, we can use the beam divergence (equal to the collection angle in bright-field imaging mode) as an upper bound to estimate the required transverse emittance. With a density of $100e/(10\,\mathrm{nm})^2$ and a total charge of 0.6 pC, the rms spot size of the full beam at the sample must be smaller than 0.5 μm. Note that the dose on the sample for this resolution will be lower than the damage threshold [19.163]. As we push the spatial resolution to 1 nm and beyond, dealing with the damage will become the limiting factor in microscope design.

One of the main challenges in realizing a 10 nm–10 ps imaging system using MeV electrons lies in the control of the energy spread. A possible solution involves the use of an additional RF cavity after the gun as an energy spread compensator. At first order, the beam longitudinal phase space distribution after the gun is characterized by an almost ideally quadratic curvature, which can be compensated for using a higher harmonic RF cavity operating at the opposite, deceleration phase. Simulations indicate that this solution can provide beams with an energy spread of a few 10^{-5}. A previously proposed two-frequency RF gun is a similar concept and can partially fulfill the beam requirement for single-shot picosecond TEM [19.164]. We note that the success of the RF curvature compensation scheme relies on precise and highly stable control of the amplitudes and phases of the S-band and X-band RF sources, enabled by recent advances in RF-laser synchronization and high-stability modulator technologies.

Another challenge for single-shot MeV TEM arises from the fact that the high electron energy that conveniently limits the influence of Coulomb self-fields comes at the cost of increased magnetic rigidity. High-voltage (1–3 MeV) electron microscopes were, until the advent of aberration correction, one of the main candidates for improving the spatial resolution in TEM to the atomic level [19.165]. These machines were overburdened by large and expensive round solenoid lenses weighing up to several tons. The unfavorable scaling of solenoid focusing power as the inverse square of the electron energy poses a practical limit to the development of time-resolved electron microscopy [19.53] and calls for the introduction of very strong magnetic lenses or novel focusing elements.

One possible approach, which borrows from experience in the field of advanced accelerators, involves the use of permanent magnet quadrupole (PMQ) lenses for imaging with relativistic electrons. PMQ triplets provide a compact short-focal-length lens for use by inverse Compton scattering sources and advanced accelerator applications [19.166]. With a gradient of $> 500\,\mathrm{T/m}$ and an effective length of 1 cm, the effective focal distance of a permanent magnet triplet can be very short (slightly more than 1 cm). Another intrinsic advantage of using quadrupole magnets instead of cylindrical solenoid lenses is that the intermediate waists between the object plane and the detector plane will be elliptical, and thus less prone to degradation of image quality by stochastic Coulomb effects.

UCLA recently reported on the use of a picosecond-long 4 MeV electron beam from an RF photoinjector and a strong compact PMQ-based lens with a focal length of ≈ 1.3 cm to obtain single-shot micrographs with micrometer-scale spatial resolution [19.167]. The quadrupoles used in the experiment were found to have field gradients of nearly 600 T/m. Magnification factors larger than 30× have been achieved. These results represent the first example of single-shot picosecond time-resolved transmission electron microscopy.

A picture of one of the assembled PMQs, along with the full triplet setup, is shown in Fig. 19.18. The total weight of the PMQs and the flexure stage is less than

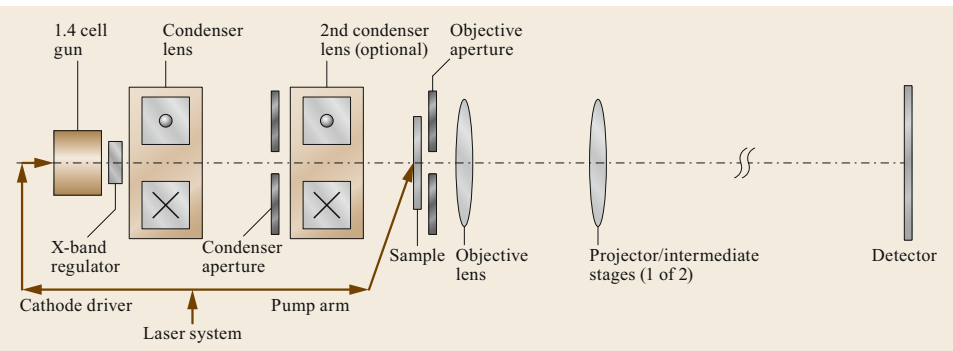

Fig. 19.17 The MeV microscope column. After [19.108]

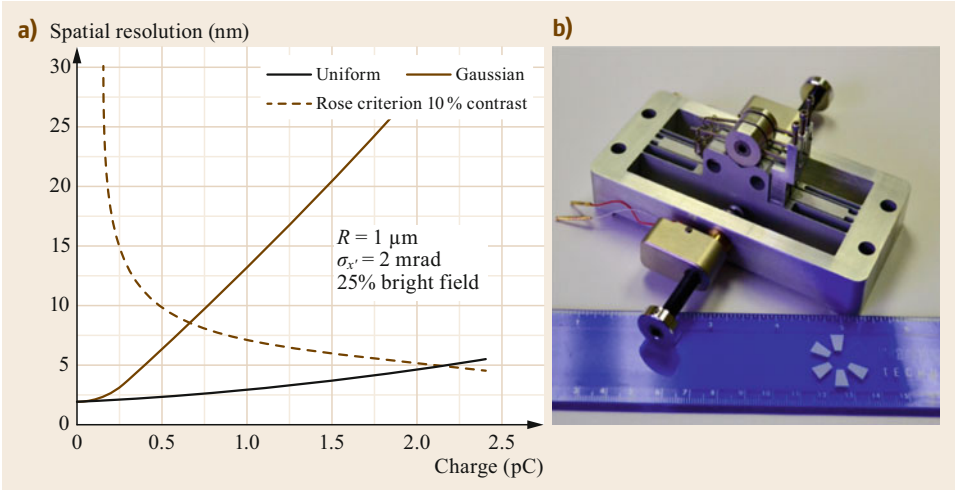

Fig. 19.18 **(a)** Spatial resolution as a function of beam charge for single-shot MeV microscope. **(b)** Permanent magnet quadrupole triplet used in the UCLA experiments

two pounds. The wedge magnetization orientations and the magnetic field in the central plane of the quadrupole are also displayed. Field maps for each of the fabricated magnets (including the individual wedge dimensions and the gaps originating from manufacturing errors) were obtained using 3-D magnetostatic simulations.

The calculated spherical aberrations for the manufactured PMQs are 8.9 and 75.2 mm in the horizontal and vertical planes, respectively. The asymmetry can be reversed by using the vertically focusing rather than the horizontally focusing quadrupole first. It was also found that for each quadrupole, an angular misalignment of $\pm 10\,\mu$rad and a transverse displacement of $50\,\mu$m relative to the central beam trajectory were required in order to avoid degradation of image quality.

When e–e interactions are taken into account, the size of the image disk of a point source is not merely determined by the collection angle, beam energy spread, and the intrinsic aberrations of the electron lenses. In fact, e–e interactions may actually distort or even wash out the information of the sample imprinted in the beam phase space as the beam propagates from the sample to the detector plane. e–e interactions in a beam can be represented by the sum of the smooth space charge forces and the stochastic scattering resulting from point-to-point discrete particle interactions [19.130]. In principle, both components of e–e interactions are inherently included in full-scale (i. e., one macroparticle in simulation for one real electron) particle tracking using a pairwise interaction model, and could be precisely modeled taking advantage of recent remarkable advances in scientific computing. Nevertheless, it still requires a significant amount of computational resources and time to track a beam with 10^7 electrons through the microscope column even for a single run, and multiple runs are necessary to reveal the scaling with relevant parameters and to guide the design and optimization of the microscope.

19.4.2 MeV Micro- and Nano-UED

Thus far, the main focus in UED instrumentation development has been to achieve continuously improved temporal resolution. The priority is reducing the pulse duration of electron beams, and some or all of the other beam parameters, including the bunch charge, spot size, divergence, and energy spread, then need to be controlled—and in some cases compromised—to match the requirements for the samples/experiments. Typical probe spot sizes in both keV and MeV UED experiments have been around $100\,\mu$m.

It is actually extremely technically challenging to prepare such large-area single-crystal samples to match the probe size. For isolated single-crystal samples, if the sample size is smaller than the probe size, the diffraction signal scales with the area of the sample size, and the unscattered electrons will obviously not contribute to the diffraction signal. For polycrystalline samples, if we wish to measure the orientation-dependent dynamics from each individual domain, the probe size must not exceed the size of that particular domain, so as to avoid signal from its neighbors. For this type of measurement, the probe size should typically be at the micrometer level or smaller, i. e., orders of magnitude smaller than those in existing UEDs. On the other hand, a traditional strength of TEM is the small probe size, as electrons can be easily focused by electromagnetic lenses to μm to pm size, but the TEM electron beams are continuous-wave and at extremely low current.

Thus, the ability to combine the strengths of UED and TEM (i. e., fs pulse duration/temporal resolution

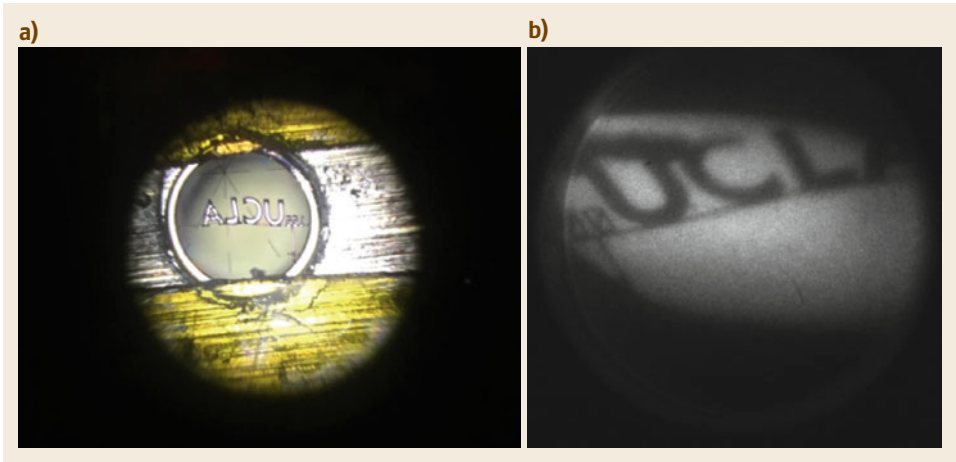

Fig. 19.19 (**a**) Optical and (**b**) electron image of the nanofabricated target employed in the UCLA experiments. Reprinted with permission from [19.167]. Copyright 2016 by the American Physical Society

with μm and smaller probe size) provides an exciting research and development opportunity, enabling studies of ultrafast structural dynamics of single domains. Micro-UED, i. e., UED with μm probe size, is complementary to XFEL, where the probe size is also at the μm level. Electrons are well suited for high-Q-resolution diffraction measurement of nm-thin samples due to the large cross section. Electrons are also preferred for studying reversible processes of single domains and biological samples with repetitive-pump–probe events due to the much lower radiation damage. With further development to reduce the probe size to the nm level, electron-based techniques will have the unique capability to access single domains and individual nanoparticles. Note that it is extremely challenging to generate nm-sized x-ray probes.

Micro- to nano-UED sets stringent requirements on the normalized emittance of the electron beams to achieve the desired probe size and Q-resolution. Assuming that the probe size is $\sigma_x = 1\,\mu\text{m}$ rms and the beam divergence is $\sigma_{x'} = 100\,\mu\text{rad}$ rms with $\gamma = 10$ electrons, the corresponding normalized emittance is $\epsilon_\text{n} = \gamma\sigma_x\sigma_{x'} = 1\,\text{nm rad}$ and the Q-resolution is $\Delta s = 2\pi\sigma_{x'}/\lambda = 0.26\,\text{Å}^{-1}$, where $\lambda = 0.24\,\text{pm}$ is the de Broglie wavelength.

The generation of 1 nm rad emittance electron beams from a flat cathode will become feasible by pushing the limits of both photocathode and drive-laser techniques. It was recently demonstrated that the intrinsic cathode emittance can be as low as 0.2 mm mrad/mm emission size from a cooled cathode material [19.168]. If the drive-laser spot size on the cathode can be reduced to 5 μm rms, the initial beam emittance will be 1 nm rad. To reach 5 μm rms laser spot size on the cathode, one needs to place the final focusing lens very close to the cathode—either through the oblique-incidence viewport of typical 1.6-cell S-band guns, or through back-illumination for novel transparent cathodes and guns [19.169, 170]. With a high acceleration-gradient electron source, one can generate and transport a bunch charge of approximately 10^4 electrons, while avoiding space-charge-induced emittance growth, and at the same time achieve 100 fs bunch length at the sample location with an RF compression technique.

If probe sizes less than 1 μm are desired, then one needs to apply collimation following a flat photocathode or starting from tip sources. Photoemission tip sources can generate lower initial emittance due to the extremely small (down to nm) emission area, even though the initial divergence is huge. The associated challenge is that with reduced emittance, the bunch charge reaching the sample will be scaled down regardless of the collimation or tip source technique, and quickly approaches the few- or even single-electron-per-pulse regime. Note that for a given beam brightness, the bunch charge scales with the square of the beam emittance. When operating in the few- or single-electron-per-pulse regime, a high pump–probe repetition rate is naturally preferred to build up the signal-to-noise ratio and statistics within a reasonable measurement time.

19.4.3 MeV Electron Energy-Loss Spectroscopy

Time-resolved EELS has recently been demonstrated in ultrafast electron microscopy (UEM), with unique capabilities such as mapping ultrafast electronic dynamics in solids and coherent quantum manipulation of free electrons in the optical near field [19.171–176]. The technique is complementary to spectroscopy measurement using x-ray free-electron lasers (FEL) and is well suited for very thin samples due to the much stronger interaction of electrons with the material. Also, the probe

size of electron beams can be focused by electromagnetic lenses to nm scale or smaller to provide detailed mapping of materials at the atomic level [19.177].

Existing UEM instruments are based on modifying commercial transmission electron microscopes to operate with pulsed electron beams generated through photoemission instead of original continuous-wave thermionic or field emission. It is extremely challenging to achieve the desired energy and temporal resolution in time-resolved EELS measurement, i. e., to minimize the energy spread and bunch length of electron beams, respectively, both of which can be severely degraded by electron–electron (e–e) interactions. The solution is to operate these instruments with extremely low charge density—on average a single electron per pulse—to eliminate the effects of e–e interactions. The typical energy resolution of these modes of operation are 1–2 eV [19.171–173, 175, 176]. Unfortunately, however, the photoelectrons have an initial energy spread of a few tenths of an eV, which translates into a bunch length of several hundred fs due to vacuum dispersion [19.174, 176], whereas a bunch length at least one order of magnitude shorter is desired to capture the fast dynamics of electronic structures.

To tackle the challenges associated with vacuum dispersion, an electron source with a significantly higher acceleration gradient and higher output energy would be necessary. Radio-frequency (RF) photocathode guns, featuring 10 s to 100 MV/m gradient and several MeV beam energy, would be the ideal choice. These sources were recently optimized for ultrafast electron diffraction [19.39, 40, 42–44, 47, 49, 50, 52, 144, 179–181] and imaging [19.53, 108], with transformative effects through the delivery of unprecedented temporal and reciprocal-spacespace/real-space resolution. Unfortunately, the energy stability of the electron beams from RF guns, as determined by the stability of the driving RF power sources, is currently at best 1×10^{-5}, i. e., 50 eV for 5 MeV beams, which is far from adequate for spectroscopy applications. Thus, unless some technical breakthrough can improve RF stability by at least two orders of magnitude, it is impractical to consider photocathode RF guns for fs EELS.

It was recently proposed that the use of a *reference beam technique* could significantly relax the stringent RF stability requirements, and the feasibility of fs MeV EELS based on RF photocathode electron sources was demonstrated. The conceptual schematic of a fs MeV EELS system is shown in Fig. 19.20. Two electron beams, referred to as the *probe beam* and *reference beam*, are generated from the photocathode with both transverse (100 μm) and longitudinal (time, 1 ps) separations. The energies of the two electron beams will fluctuate at the 50 eV level (1×10^{-5} of 5 MeV) due to the stability of the RF power source. However, the *difference* between their energies and the energy spread of each individual beam can all be controlled at the sub-0.1 eV level.

At the sample location, the two beams are also transversely (vertically) separated, and only the *probe beam* will interact with the sample. The longitudinal separation is necessary to minimize e–e interaction effects at transverse focus. A high-resolution spectrometer will record both the scattered *probe beam* and the unperturbed *reference beam*. The energy difference between the two beams is twofold: the energy loss due to the sample, and the original energy difference when the sample is not present. By recording the probe and reference beam pair on a shot-by-shot basis and comparing the energy difference, one can construct a complete energy-loss spectrum from the sample. Note that the original energy difference contributes as a fixed offset of the zero-loss peak and does not cause any distortion of the energy axis.

Simulation results show that sub-eV energy resolution can be achieved even with 50 eV beam energy

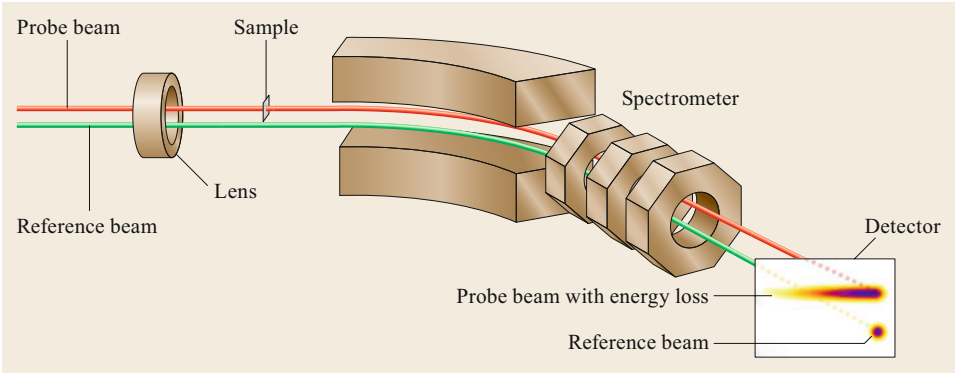

Fig. 19.20 Concept of the *reference beam* scheme for femtosecond MeV EELS based on RF photocathode guns. Reprinted with permission from [19.178] Copyright 2017 by the American Physical Society

fluctuation. Meanwhile, the temporal resolution is improved to the 10 fs level, which is more than one order of magnitude beyond the state of the art. One may also take advantage of the MeV beam energy to study thicker samples, due to the reduced inelastic cross section compared with commonly used 200–300 keV electrons. Or, for the same sample thickness, multiple scattering will be reduced with MeV electrons, which greatly simplifies the interpretation of the EELS spectrum.

The success of fs MeV EELS will rely on the generation and preservation of sub-eV energy spread, 10 fs bunch length, and sub-nm emittance electron beams from the source, through the sample, and up to the spectrometer. Such a precisely shaped and miniature phase space volume can accommodate only a single electron per pulse. A high-repetition-rate electron source is a natural choice to build up a high signal-to-noise ratio within a reasonable data acquisition time. Under circumstances where the pump–probe repetition rate is limited to GHz due to laser-induced sample hearing, a pulsed RF gun is also an option with $> 100\,\mathrm{MV/m}$ to deliver the shortest electron-beam pulse duration.

Acknowledgments. Pietro Musumeci would like to acknowledge graduate student E. Cropp (partially supported by the National Science Foundation under Grant No. DMR 1548924) who patiently helped with final editing and sorting of the references.

References

19.1 J. Hemminger, G. Fleming, M. Ratner: *Directing Matter and Energy: Five Challenges for Science and the Imagination*, Report from the Basic Energy Sciences Advisory Committee (Dept. of Energy, Washington 2007)

19.2 J. Hemminger, J. Sarrao, G. Crabtree, G. Fleming, M. Ratner: *Challenges at the Frontiers of Matter and Energy: Transformative Opportunities for Discovery Science*, Report from the Basic Energy Sciences Advisory Committee (Dept. of Energy, Washington 2015)

19.3 E. Hall, S. Stemmer, H. Zheng, Y. Zhu, G. Maracas: *Future of Electron Scattering and Diffraction* (Dept. of Energy, Washington 2014)

19.4 W.E. King, G.H. Campbell, A. Frank, B. Reed, J.F. Schmerge, B.J. Siwick, B.C. Stuart, P.M. Weber: Ultrafast electron microscopy in materials science, biology, and chemistry, J. Appl. Phys. **97**(11), 111101 (2005)

19.5 F. Carbone, P. Musumeci, O.J. Luiten, C. Hebert: A perspective on novel sources of ultrashort electron and x-ray pulses, Chem. Phys. **392**(1), 1 (2012)

19.6 F. Schotte, M. Lim, T.A. Jackson, A.V. Smirnov, J. Soman, J.S. Olson, G.N. Phillips, M. Wulff, P.A. Anfinrud: Watching a protein as it functions with 150-ps time-resolved x-ray crystallography, Science **300**(5627), 1944 (2003)

19.7 A.H. Zewail: Femtochemistry: Atomic-scale dynamics of the chemical bond, J. Phys. Chem. A **104**(24), 5660 (2000)

19.8 T. Brabec, F. Krausz: Intense few-cycle laser fields: Frontiers of nonlinear optics, Rev. Mod. Phys. **72**(2), 545 (2000)

19.9 T. Pfeifer, C. Spielmann, G. Gerber: Femtosecond x-ray science, Rep. Prog. Phys. **69**(2), 443 (2006)

19.10 D.H. Bilderback, P. Elleaume: Review of third and next generation synchrotron light sources, J. Phys. B **38**(9), S773 (2005)

19.11 C. Bostedt, J.D. Bozek, P.H. Bucksbaum, R.N. Coffee, J.B. Hastings, Z. Huang, R.W. Lee, S. Schorb, J.N. Corlett, P. Denes, P. Emma, R.W. Falcone, R.W. Schoenlein, G. Doumy, E.P. Kanter, B. Kraessig, S. Southworth, L. Young, L. Fang, M. Hoener, N. Berrah, C. Roedig, L.F. DiMauro: Ultra-fast and ultra-intense x-ray sciences: First results from the Linac Coherent Light Source free-electron laser, J. Phys. B **46**(16), 164003 (2013)

19.12 C. Bostedt, S. Boutet, D.M. Fritz, Z. Huang, H.J. Lee, H.T. Lemke, A. Robert, W.F. Schlotter, J.J. Turner, G.J. Williams: Linac Coherent Light Source: The first five years, Rev. Mod. Phys. **88**(1), 015007 (2016)

19.13 J. Spence: X-ray imaging: Ultrafast diffract-and-destroy movies, Nat. Photonics **2**(7), 390 (2008)

19.14 R. Henderson: Realizing the potential of electron cryo-microscopy, Q. Rev. Biophys. **37**(1), 3 (2004)

19.15 F. Vigliotti, S. Chen, C.-Y. Ruan, V.A. Lobastov, A.H. Zewail: Ultrafast electron crystallography of surface structural dynamics with atomic-scale resolution, Angew. Chem. **43**, 2705–2709 (2004)

19.16 G. Mourou, S. Williamson: Picosecond electron diffraction, Appl. Phys. Lett. **41**(1), 44 (1982)

19.17 A.A. Ischenko, S.A. Aseyev (Eds.): *Time-Resolved Electron Diffraction*, Advances in Imaging and Electron Physic, Vol. 184 (Elsevier, Amsterdam 2014)

19.18 A.H. Zewail: 4-D ultrafast electron diffraction, crystallography, and microscopy, Annu. Rev. Phys. Chem. **57**(1), 65 (2006)

19.19 G. Sciaini, R.J.D. Miller: Femtosecond electron diffraction: Heralding the era of atomically resolved dynamics, Rep. Prog. Phys. **74**(9), 096101 (2011)

19.20 P. Gallant, P. Forget, F. Dorchies, Z. Jiang, J.C. Kieffer, P.A. Jaanimagi, J.C. Rebuffie, C. Goulmy, J.F. Pelletier, M. Sutton: Characterization of a subpicosecond x-ray streak camera for ultrashort laser-produced plasmas experiments, Rev. Sci. Instrum. **71**(10), 3627 (2000)

19.21 B.J. Siwick, J.R. Dwyer, R.E. Jordan, R.J.D. Miller: Ultrafast electron optics: Propagation dynamics of femtosecond electron packets, J. Appl. Phys. **92**(3), 1643 (2002)

19.22 B.W. Reed: Femtosecond electron pulse propagation for ultrafast electron diffraction, J. Appl. Phys. **100**(3), 034916 (2006)

19.23 J. Cao, Z. Hao, H. Park, C. Tao, D. Kau, L. Blaszczyk: Femtosecond electron diffraction for direct measurement of ultrafast atomic motions, Appl. Phys. Lett. **83**(5), 1044 (2003)

19.24 B.J. Siwick, J.R. Dwyer, R.E. Jordan, R.J.D. Miller: An atomic-level view of melting using femtosecond electron diffraction, Science **302**(5649), 1382 (2003)

19.25 L. Waldecker, R. Bertoni, R. Ernstorfer: Compact femtosecond electron diffractometer with 100 keV electron bunches approaching the single-electron pulse duration limit, J. Appl. Phys. **117**(4), 044903 (2015)

19.26 P. Baum: On the physics of ultrashort single-electron pulses for time-resolved microscopy and diffraction, Chem. Phys. **423**, 55 (2013)

19.27 R. Ernstorfer, M. Harb, C.T. Hebeisen, G. Sciaini, T. Dartigalongue, R.J.D. Miller: The formation of warm dense matter: Experimental evidence for electronic bond hardening in gold, Science **323**(5917), 1033 (2009)

19.28 R.C. Dudek, P.M. Weber: Ultrafast diffraction imaging of the electrocyclic ring-opening reaction of 1,3-cyclohexadiene, J. Phys. Chem. A **105**(17), 4167 (2001)

19.29 H. Ihee, V.A. Lobastov, U.M. Gomez, B.M. Goodson, R. Srinivasan, C.-Y. Ruan, A.H. Zewail: Direct imaging of transient molecular structures with ultrafast diffraction, Science **291**(5503), 458 (2001)

19.30 F. Carbone, P. Baum, P. Rudolf, A.H. Zewail: Structural preablation dynamics of graphite observed by ultrafast electron crystallography, Phys. Rev. Lett. **100**(3), 139901 (2008)

19.31 N. Gedik, D.S. Yang, G. Logvenov, I. Bozovic, A.H. Zewail: Nonequilibrium phase transitions in cuprates observed by ultrafast electron crystallography, Science **316**(5823), 425 (2007)

19.32 T. Ishikawa, S.A. Hayes, S. Keskin, G. Corthey, M. Hada, K. Pichugin, A. Marx, J. Hirscht, K. Shionuma, K. Onda, Y. Okimoto, S.Y. Koshihara, T. Yamamoto, H. Cui, M. Nomura, Y. Oshima, M. Abdel-Jawad, R. Kato, R.J.D. Miller: Direct observation of collective modes coupled to molecular orbital-driven charge transfer, Science **350**(6267), 1501 (2015)

19.33 M. Eichberger, H. Schäfer, M. Krumova, M. Beyer: Snapshots of cooperative atomic motions in the optical suppression of charge density waves, Nature **468**(7325), 799 (2010)

19.34 T. van Oudheusden, E.F. De Jong, S.B. van der Geer, W.P.E.M. Op 't Root, O.J. Luiten, B.J. Siwick: Electron source concept for single-shot sub-100 fs electron diffraction in the 100 keV range, J. Appl. Phys. **102**(9), 093501 (2007)

19.35 X.J. Wang, X. Qiu, I. Ben-Zvi: Experimental observation of high-brightness microbunching in a photocathode RF electron gun, Phys. Rev. E **54**, R3121 (1996)

19.36 T. van Oudheusden, P.L.E.M. Pasmans, S.B. van der Geer, M.J. de Loos, M.J. van der Wiel, O.J. Luiten: Compression of subrelativistic space-charge-dominated electron bunches for single-shot femtosecond electron diffraction, Phys. Rev. Lett. **105**(26), 264801 (2010)

19.37 R.P. Chatelain, V.R. Morrison, C. Godbout, B.J. Siwick: Ultrafast electron diffraction with radio-frequency compressed electron pulses, Appl. Phys. Lett. **101**(8), 081901 (2012)

19.38 D. Alesini, A. Battisti, M. Ferrario, L. Foggetta, V. Lollo, L. Ficcadenti, V. Pettinacci, S. Custodio, E. Pirez, P. Musumeci: New technology based on clamping for high gradient radio frequency photogun, Phys. Rev. ST Accel. Beams **18**(9), 092001 (2015)

19.39 X.J. Wang, Z. Wu, H. Ihee: Potential of femtosecond relativistic electron diffraction. In: *Proc. 2003 Part. Accel. Conf.* (2003) p. 420

19.40 X.J. Wang, D. Xiang, T.K. Kim, H.H. Ihee: Potential of femtosecond electron diffraction using near-relativistic electrons from a photocathode RF electron gun, J. Korean Phys. Soc. **48**(3), 390–396 (2006)

19.41 R. Akre, D. Dowell, P. Emma, J. Frisch, S. Gilevich: Commissioning the Linac Coherent Light Source injector, Phys. Rev. ST Accel. Beams **11**(3), 030703 (2008)

19.42 J.B. Hastings, F.M. Rudakov, D.H. Dowell, J.F. Schmerge, J.D. Cardoza, J.M. Castro, S.M. Gierman, H. Loos, P.M. Weber: Ultrafast time-resolved electron diffraction with megavolt electron beams, Appl. Phys. Lett. **89**(18), 184109 (2006)

19.43 P. Musumeci, J.T. Moody, C.M. Scoby: Relativistic electron diffraction at the UCLA Pegasus photoinjector laboratory, Ultramicroscopy **108**(11), 1450 (2008)

19.44 R. Li, C. Tang, Y. Du, W. Huang, Q. Du, J. Shi, L. Yan, X. Wang: Experimental demonstration of high quality MeV ultrafast electron diffraction, Rev. Sci. Instrum. **80**(8), 083303 (2009)

19.45 P. Musumeci, J.T. Moody, C.M. Scoby, M.S. Gutierrez, M. Westfall: Laser-induced melting of a single crystal gold sample by time-resolved ultrafast relativistic electron diffraction, Appl. Phys. Lett. **97**(6), 063502 (2010)

19.46 C.T. Hebeisen, G. Sciaini, M. Harb, R. Ernstorfer, T. Dartigalongue, S.G. Kruglik, R.J.D. Miller: Grating enhanced ponderomotive scattering for visualization and full characterization of femtosecond electron pulses, Opt. Express **16**(5), 3334 (2008)

19.47 Y. Murooka, N. Naruse, S. Sakakihara, M. Ishimaru, J. Yang, K. Tanimura: Transmission-electron diffraction by MeV electron pulses, Appl. Phys. Lett. **98**(25), 251903 (2011)

19.48 P. Zhu, Y. Zhu, Y. Hidaka, L. Wu, J. Cao: Femtosecond time-resolved MeV electron diffraction, New J. Phys. **17**(6), 063004 (2015)

19.49 S. Manz, A. Casandruc, D. Zhang, Y. Zhong: Mapping atomic motions with ultrabright electrons: Towards fundamental limits in space-time resolution, Faraday Discuss. **177**, 467 (2015)

19.50 S.P. Weathersby, G. Brown, M. Centurion, T.F. Chase, R. Coffee, J. Corbett, J.P. Eichner, J.C. Frisch, A.R. Fry, M. Gühr, N. Hartmann, C. Hast, R. Hettel, R.K. Jobe, E.N. Jongewaard, J.R. Lewandowski, R.K. Li, A.M. Lindenberg, I. Makasyuk, J.E. May, D. McCormick, M.N. Nguyen, A.H. Reid, X. Shen, K. Sokolowski-Tinten, T. Vecchione, S.L. Vetter, J. Wu, J. Yang, H.A. Dürr, X.J. Wang: Mega-electron-volt ultrafast electron diffraction at SLAC National Accelerator Laboratory, Rev. Sci. Instrum. **86**(7), 073702 (2015)

19.51 L.W. Feng, L. Lin, S.L. Huang, S.W. Quan, T. Jiang, P.F. Zhu, J.K. Hao, F. Zhu, F. Wang, F. Fu, R. Wang, L. Zhao, D. Xiang, K.X. Liu: Ultrafast electron diffraction with megahertz MeV electron pulses from a superconducting radio-frequency photoinjector, Appl. Phys. Lett. **107**(22), 224101 (2015)

19.52 D. Filippetto, H. Qian: Design of a high-flux instrument for ultrafast electron diffraction and microscopy, J. Phys. B **49**(10), 104003 (2016)

19.53 D. Xiang, F. Fu, J. Zhang, X. Huang, L. Wang, X. Wang, W. Wan: Accelerator-based single-shot ultrafast transmission electron microscope with picosecond temporal resolution and nanometer spatial resolution, Nucl. Instrum. Methods Phys. Res. A **759**, 74 (2014)

19.54 B. Hou, V. Malka, K. Krushelnick, J. Faure: Electron diffraction using ultrafast electron bunches from a laser-wakefield accelerator at kHz repetition rate, Appl. Phys. Lett. **102**(6), 064104 (2013)

19.55 F. Salvat, J.D. Martnez, R. Mayol, J. Parellada: Analytical Dirac-Hartree-Fock-Slater screening function for atoms ($Z = 1-92$), Phys. Rev. A **36**(2), 467 (1987)

19.56 F. Salvat, R. Mayol: Elastic scattering of electrons and positrons by atoms. Schrödinger and Dirac partial wave analysis, Comput. Phys. Commun. **74**(3), 358 (1993)

19.57 H. Shinotsuka, S. Tanuma, C.J. Powell, D.R. Penn: Calculations of electron inelastic mean free paths. X. Data for 41 elemental solids over the 50 eV to 200 keV range with the relativistic full Penn algorithm, Surf. Interface Anal. **47**(9), 871 (2015)

19.58 L. Reimer: *Transmission Electron Microscopy: Physics of Image Formation and Microanalysis*, Springer Series in Optical Sciences, Vol. 36 (Springer, New York 2013)

19.59 J.C.H. Spence: Outrunning damage: Electrons vs. x-rays-timescales and mechanisms, Struct. Dyn. **4**(4), 044027 (2017)

19.60 P. Grivet, P.W. Hawkes, A. Septier: *Electron Optics*, 2nd edn. (Pergamon, New York 1972)

19.61 C.A. Brau: What brightness means. In: *The Physics and Applications of High Brightness Electron Beams*, ed. by J. Rosenzweig, G. Travish, L. Serafini (World Scientific, Singapore 2003) p. 20

19.62 G.H. Jansen: Coulomb interactions in particle beams, J. Vac. Sci. Technol. B **6**(6), 1977 (1988)

19.63 J.T. Moody, P. Musumeci, M.S. Gutierrez, J.B. Rosenzweig, C.M. Scoby: Longitudinal phase space characterization of the blow-out regime of RF photoinjector operation, Phys. Rev. ST Accel. Beams **12**(7), 070704 (2009)

19.64 I.V. Bazarov, B.M. Dunham, C.K. Sinclair: Maximum achievable beam brightness from photoinjectors, Phys. Rev. Lett. **102**(10), 104801 (2009)

19.65 D. Filippetto, P. Musumeci, M. Zolotorev, G. Stupakov: Maximum current density and beam brightness achievable by laser-driven electron sources, Phys. Rev. ST Accel. Beams **17**(2), 024201 (2014)

19.66 I.V. Bazarov, C.K. Sinclair: Multivariate optimization of a high brightness DC gun photoinjector, Phys. Rev. ST Accel. Beams **8**(3), 034202 (2005)

19.67 P. Musumeci, J.T. Moody, R.J. England, J.B. Rosenzweig, T. Tran: Experimental generation and characterization of uniformly filled ellipsoidal electron-beam distributions, Phys. Rev. Lett. **100**(24), 244801 (2008)

19.68 J.B. Rosenzweig, A. Cahill, V. Dolgashev, C. Emma, A. Fukusawa, R. Li, C. Limborg, J. Maxson, P. Musumeci, A. Nause, R. Pakter, R. Pompili, R. Roussel, B. Spataro, S. Tantawi: Next generation high brightness electron beams from ultra-high field cryogenic radiofrequency photocathode sources, arXiv:1603.01657 [physics.acc-ph] (2016)

19.69 Y. Ding, A. Brachmann, F.J. Decker, D. Dowell, P. Emma, J. Frisch, S. Gilevich, G. Hays, P. Hering, Z. Huang, R. Iverson, H. Loos, A. Miahnahri, H.D. Nuhn, D. Ratner, J. Turner, J. Welch, W. White, J. Wu: Measurements and simulations of ultralow emittance and ultrashort electron beams in the Linac Coherent Light Source, Phys. Rev. Lett. **102**(25), 254801 (2009)

19.70 A. Arnold, M. Freitag, P. Murcek, J. Teichert, H. Vennekate, R. Xiang, P. Kniesel, P. Lu, M. Stirbet, G. Ciovati, L. Turhington: RF performance results of the 2nd ELBE SRF gun. In: *Proc. SRF2015* (2015) p. THPB055

19.71 D.T. Palmer: *The Next Generation Photoinjector*, Ph.D. Thesis (Stanford University, Stanford 1998)

19.72 T. Schietinger, M. Pedrozzi, M. Aiba, V. Arsov, S. Bettoni, B. Beutner, M. Calvi, P. Craievich, M. Dehler, F. Frei: Commissioning experience and beam physics measurements at the SwissFEL injector test facility, Phys. Rev. Accel. Beams **19**(10), 100702 (2016)

19.73 P. Musumeci, L. Faillace, A. Fukasawa: Novel radio-frequency gun structures for ultrafast relativistic electron diffraction, Microsc. Microanal. **15**(4), 290 (2009)

19.74 A. Fukasawa, H. To, S.K. Mahapatra, B. Baumgartner, A. Cahill, K. Fitzmorris, R. Li, P. Musumeci, J.B. Rosenzweig, B. Spataro, D. Alesini, L. Ficcadenti, A. Valloni, L. Palumbo: Progress on the

hybrid gun project at UCLA, Phys. Procedia **52**, 2 (2014)
19.75 E. Pirez, P. Musumeci, J. Maxson, D. Alesini: S-band 1.4 cell photoinjector design for high brightness beam generation, Nucl. Instrum. Methods Phys. Res. A **865**, 109 (2016)
19.76 F. Sannibale, D. Filippetto, C.F. Papadopoulos, J. Staples, R. Wells, B. Bailey, K. Baptiste, J. Corlett, C. Cork, S. De Santis: Advanced photoinjector experiment photogun commissioning results, Phys. Rev. ST Accel. Beams **15**(10), 103501 (2012)
19.77 A. Arnold, J. Teichert: Overview on superconducting photoinjectors, Phys. Rev. ST Accel. Beams **14**(2), 024801 (2011)
19.78 E. Esarey, C.B. Schroeder, W.P. Leemans: Physics of laser-driven plasma-based electron accelerators, Rev. Mod. Phys. **81**(3), 1229 (2009)
19.79 O. Lundh, J. Lim, C. Rechatin, L. Ammoura, A. Ben-Ismail, X. Davoine, G. Gallot, J.-P. Goddet, E. Lefebvre, V. Malka: Few femtosecond, few kiloampere electron bunch produced by a laser-plasma accelerator, Nat. Phys. **7**(3), 219 (2011)
19.80 J. Faure, B. van der Geer, B. Beaurepaire, G. Gallé, A. Vernier, A. Lifschitz: Concept of a laser-plasma-based electron source for sub-10-fs electron diffraction, Phys. Rev. Accel. Beams **19**(2), 021302 (2016)
19.81 Z.-H. He, A.G.R. Thomas, B. Beaurepaire, J.A. Nees, B. Hou, V. Malka, K. Krushelnick, J. Faure: Electron diffraction using ultrafast electron bunches from a laser-wakefield accelerator at kHz repetition rate, Appl. Phys. Lett. **102**(6), 064104 (2013)
19.82 D.H. Dowell, I. Bazarov, B. Dunham, K. Harkay, C. Hernandez-Garcia, R. Legg, H. Padmore, T. Rao, J. Smedley, W. Wan: Cathode R&D for future light sources, Nucl. Instrum. Methods Phys. Res. A **622**(3), 685 (2010)
19.83 J. Maxson, H. Lee, A.C. Bartnik, J. Kiefer, I. Bazarov: Adaptive electron beam shaping using a photoemission gun and spatial light modulator, Phys. Rev. ST Accel. Beams **18**(2), 023401 (2015)
19.84 D.H. Dowell, J.F. Schmerge: Quantum efficiency and thermal emittance of metal photocathodes, Phys. Rev. ST Accel. Beams **12**(7), 074201 (2009)
19.85 M.C. Divall, E. Prat, S. Bettoni, C. Vicario, A. Trisorio, T. Schietinger, C.P. Hauri: Intrinsic emittance reduction of copper cathodes by laser wavelength tuning in an RF photoinjector, Phys. Rev. ST Accel. Beams **18**(3), 033401 (2015)
19.86 J.M. Maxson, I.V. Bazarov, W. Wan, H.A. Padmore, C.E. Coleman-Smith: Fundamental photoemission brightness limit from disorder induced heating, New J. Phys. **15**(10), 103024 (2013)
19.87 S. Karkare, I. Bazarov: Effects of surface nonuniformities on the mean transverse energy from photocathodes, Phys. Rev. Appl. **4**(2), 024015 (2015)
19.88 L. Cultrera, S. Karkare, H. Lee, X. Liu, I. Bazarov, B. Dunham: Cold electron beams from cryocooled, alkali antimonide photocathodes, Phys. Rev. ST Accel. Beams **18**(11), 113401 (2015)
19.89 D.T. Pierce, F. Meier, P. Zürcher: Negative electron affinity GaAs: A new source of spin-polarized electrons, Appl. Phys. Lett. **26**(12), 670 (1975)
19.90 J. Maxson, D. Cesar, G. Calmasini, A. Ody, P. Musumeci, D. Alesini: Direct measurement of sub-10 fs relativistic electron beams with ultralow emittance, Phys. Rev. Lett. **118**(15), 154802 (2016)
19.91 M.J. de Loos, S.B. van der Geer, Y.M. Saveliev, V.M. Pavlov, A.J.W. Reitsma, S.M. Wiggins, J. Rodier, T. Garvey, D.A. Jaroszynski: Radial bunch compression: Path-length compensation in an RF photoinjector with a curved cathode, Phys. Rev. ST Accel. Beams **9**(8), 084201 (2006)
19.92 K. Floettmann, V.V. Paramonov: Beam dynamics in transverse deflecting RF structures, Phys. Rev. ST Accel. Beams **17**(2), 024001 (2014)
19.93 P. Musumeci, H.A. Bender, N.S. Wilcox: Imaging single electrons to enable the generation of ultrashort beams for single-shot femtosecond relativistic electron diffraction, J. Appl. Phys. **110**(7), 074512 (2011)
19.94 Y. Glinec, J. Faure, A. Guemnie-Tafo, V. Malka, H. Monard, J.P. Larbre, V. De Waele, J.L. Marignier, M. Mostafavi: Absolute calibration for a broad range single shot electron spectrometer, Rev. Sci. Instrum. **77**(10), 103301 (2006)
19.95 A. Buck, K. Zeil, A. Popp, K. Schmid, A. Jochmann, S.D. Kraft, B. Hidding, T. Kudyakov, C.M.S. Sears, L. Veisz, S. Karsch, J. Pawelke, R. Sauerbrey, T. Cowan, F. Krausz, U. Schramm: Absolute charge calibration of scintillating screens for relativistic electron detection, Rev. Sci. Instrum. **81**(3), 033301 (2010)
19.96 R.K. Li, P. Musumeci, H.A. Bender, N.S. Wilcox, M. Wu: Imaging single electrons to enable the generation of ultrashort beams for single-shot femtosecond relativistic electron diffraction, J. Appl. Phys. **110**(7), 074512 (2011)
19.97 R. Ischebeck, E. Prat, V. Thominet, C.O. Loch: Transverse profile imager for ultrabright electron beams, Phys. Rev. ST Accel. Beams **18**(8), 082802 (2015)
19.98 M.W. Tate, P. Purohit, D. Chamberlain, K.X. Nguyen, R.M. Hovden, C.S. Chang, P. Deb, E. Turgut, J.T. Heron, D.G. Schlom, D.C. Ralph, G.D. Fuchs, K.S. Shanks, H.T. Philipp, D.A. Muller, S.M. Gruner: High dynamic range pixel array detector for scanning transmission electron microscopy, Microsc. Microanal. **22**, 237 (2016)
19.99 E. Nogales: The development of cryo-EM into a mainstream structural biology technique, Nat. Methods **13**(1), 24 (2015)
19.100 M. Battaglia, D. Contarato, P. Denes, P. Giubilato: Cluster imaging with a direct detection CMOS pixel sensor in transmission electron microscopy, Nucl. Instrum. Methods Phys. Res. A **608**(2), 363 (2009)
19.101 A. Gliserin, M. Walbran, F. Krausz, P. Baum: Sub-phonon-period compression of electron pulses for atomic diffraction, Nat. Commun. **6**, 8723 (2015)
19.102 R.P. Chatelain, V.R. Morrison, B.L.M. Klarenaar, B.J. Siwick: Coherent and incoherent electron-

phonon coupling in graphite observed with radio-frequency compressed ultrafast electron diffraction, Phys. Rev. Lett. **113**(23), 235502 (2014)
19.103 K. Ishioka, M. Hase, M. Kitajima, L. Wirtz, A. Rubio, H. Petek: Ultrafast electron–phonon decoupling in graphite, Phys. Rev. B **77**(12), 121402 (2008)
19.104 S.G. Anderson, P. Musumeci, J.B. Rosenzweig, W.J. Brown, R.J. England, M. Ferrario, J.S. Jacob, M.C. Thompson, G. Travish, A.M. Tremaine: Velocity bunching of high-brightness electron beams, Phys. Rev. ST Accel. Beams **8**(1), 014401 (2005)
19.105 M. Ferrario, D. Alesini, A. Bacci, M. Bellaveglia, R. Boni, M. Boscolo, M. Castellano, E. Chiadroni, A. Cianchi, L. Cultrera: Experimental demonstration of emittance compensation with velocity bunching, Phys. Rev. Lett. **104**(5), 054801 (2010)
19.106 X.H. Lu, C.X. Tang, R.K. Li, H. To, G. Andonian, P. Musumeci: Generation and measurement of velocity bunched ultrashort bunch of pC charge, Phys. Rev. ST Accel. Beams **18**(3), 032802 (2015)
19.107 I. Dornmair, C.B. Schroeder, K. Floettmann: Plasma-driven ultrashort bunch diagnostics, Phys. Rev. ST Accel. Beams **19**(6), 062801 (2016)
19.108 R.K. Li, P. Musumeci: Single-shot MeV transmission electron microscopy with picosecond temporal resolution, Phys. Rev. Appl. **2**(2), 024003 (2014)
19.109 B. Zeitler, K. Floettmann, F. Grüner: Linearization of the longitudinal phase space without higher harmonic field, Phys. Rev. ST Accel. Beams **18**(12), 120102 (2015)
19.110 M.J. de Loos, S.B. van der Geer: General particle tracer, http://www.pulsar.nl/gpt (1996)
19.111 M. Eichberger, N. Erasmus, K. Haupt, G. Kassier, A. von Flotow, J. Demsar, H. Schwoerer: Femtosecond streaking of electron diffraction patterns to study structural dynamics in crystalline matter, Appl. Phys. Lett. **102**(12), 121106 (2013)
19.112 E. Curry, S. Fabbri, P. Musumeci, A. Gover: THz-driven zero-slippage IFEL scheme for phase space manipulation, New J. Phys. **18**(11), 113045 (2016)
19.113 P. Baum, A. Zewail: Femtosecond diffraction with chirped electron pulses, Chem. Phys. Lett. **462**(1–3), 14 (2008)
19.114 P. Musumeci, J.T. Moody, C.M. Scoby, M.S. Gutierrez, T. Tran: RF streak camera based ultrafast relativistic electron diffraction, Rev. Sci. Instrum. **80**(1), 013302 (2009)
19.115 Z.H. He, B. Beaurepaire, J.A. Nees, G. Gall, S.A. Scott, J.R.S. Perez, M.G. Lagally, K. Krushelnick, A.G.R. Thomas, J. Faure: Capturing structural dynamics in crystalline silicon using chirped electrons from a laser wakefield accelerator, Sci. Rep. **6**, 36224 (2016)
19.116 R. Li, W. Huang, Y. Du, L. Yan, Q. Du, J. Shi, J. Hua, H. Chen, T. Du, H. Xu, C. Tang: Note: Single-shot continuously time-resolved MeV ultrafast electron diffraction, Rev. Sci. Instrum. **81**(3), 036110 (2010)
19.117 N. Hartmann, W. Helml, A. Galler, M.R. Bionta, J. Grünert, S.L. Molodtsov, K.R. Ferguson, S. Schorb, M.L. Swiggers, S. Carron: Sub-femtosecond precision measurement of relative x-ray arrival time for free-electron lasers, Nat. Photonics **8**, 706709 (2014)
19.118 F. Tavella, N. Stojanovic, G. Geloni, M. Gensch: Few-femtosecond timing at fourth-generation x-ray light sources, Nat. Photonics **5**(3), 162 (2011)
19.119 E. Allaria, G. De Ninno, S. Di Mitri, W.M. Fawley, E. Ferrari, L. Fröhlich, G. Penco, P. Sigalotti, S. Spampinati, C. Spezzani: Energy slicing analysis for time-resolved measurement of electron-beam properties, Phys. Rev. ST Accel. Beams **17**(1), 010704 (2014)
19.120 J.T. Moody, P. Musumeci, G. Anderson, S. Anderson, S. Betts, S. Fisher, D. Gibson, A. Tremaine, S. Wu: The LLNL/UCLA high gradient inverse free electron laser accelerator, Energy **70**, 140 (2012)
19.121 C.M. Scoby, P. Musumeci, J.T. Moody, M.S. Gutierrez: Electro-optic sampling at 90 degree interaction geometry for time-of-arrival stamping of ultrafast relativistic electron diffraction, Phys. Rev. ST Accel. Beams **13**(2), 022801 (2010)
19.122 A. Angelovski, M. Kuntzsch, M.K. Czwalinna, A. Penirschke, M. Hansli, C. Sydlo, V. Arsov, S. Hunziker, H. Schlarb, M. Gensch: Evaluation of the cone-shaped pickup performance for low charge sub-10 fs arrival-time measurements at free electron laser facilities, Phys. Rev. ST Accel. Beams **18**(1), 012801 (2015)
19.123 M. Harmand, R. Coffee, M.R. Bionta, M. Chollet, D. French, D. Zhu, D.M. Fritz, H.T. Lemke, N. Medvedev, B. Ziaja, S. Toleikis, M. Cammarata: Achieving few-femtosecond time-sorting at hard x-ray free-electron lasers, Nat. Photonics **7**(3), 215 (2013)
19.124 A.L. Cavalieri, D.M. Fritz, S.H. Lee, P.H. Bucksbaum, D.A. Reis, J. Rudati, D.M. Mills, P.H. Fuoss, G.B. Stephenson, C.C. Kao, D.P. Siddons, D.P. Lowney, A.G. MacPhee, D. Weinstein, R.W. Falcone, R. Pahl, J. Als-Nielsen, C. Blome, S. Düsterer, R. Ischebeck, H. Schlarb, H. Schulte-Schrepping, T. Tschentscher, J. Schneider, O. Hignette, F. Sette, K. Sokolowski-Tinten, H.N. Chapman, R.W. Lee, T.N. Hansen, O. Synnergren, J. Larsson, S. Techert, J. Sheppard, J.S. Wark, M. Bergh, C. Caleman, G. Huldt, D. van der Spoel, N. Timneanu, J. Hajdu, R.A. Akre, E. Bong, P. Emma, P. Krejcik, J. Arthur, S. Brennan, K.J. Gaffney, A.M. Lindenberg, K. Luening, J.B. Hastings: Clocking femtosecond x-rays, Phys. Rev. Lett. **94**(11), 114801 (2005)
19.125 M. Gao, H. Jean-Ruel, R.R. Cooney, J. Stampe, M. de Jong, M. Harb, G. Sciaini, G. Moriena, R.J.D. Miller: Full characterization of RF compressed femtosecond electron pulses using ponderomotive scattering, Opt. Express **20**(11), 12048 (2012)
19.126 G.H. Kassier, K. Haupt, N. Erasmus, E.G. Rohwer, H.M. von Bergmann, H. Schwoerer, S.M.M. Coelho, F.D. Auret: A compact streak camera for 150 fs time resolved measurement of bright pulses in ultrafast electron diffraction, Rev. Sci. Instrum. **81**(10), 105103 (2010)

19.127 D.B. Cesar, P. Musumeci, D. Alesini: Ultrafast gating of a mid-infrared laser pulse by a sub-pC relativistic electron beam, J. Appl. Phys. **118**(23), 234506 (2015)

19.128 R. Ulbricht, E. Hendry, J. Shan, T.F. Heinz, M. Bonn: Carrier dynamics in semiconductors studied with time-resolved terahertz spectroscopy, Rev. Mod. Phys. **83**(2), 543 (2011)

19.129 A. Cavalleri, S. Wall, C. Simpson, E. Statz, D.W. Ward, K.A. Nelson, M. Rini, R.W. Schoenlein: Tracking the motion of charges in a terahertz light field by femtosecond x-ray diffraction, Nature **442**(7103), 664 (2006)

19.130 M. Reiser: *Theory and Design of Charged Particle Beams* (Wiley-VCH, Weinheim 2008)

19.131 C. Gulliford, A. Bartnik, I. Bazarov: Multiobjective optimizations of a novel cryocooled DC gun based ultrafast electron diffraction beam line, Phys. Rev. Accel. Beams **19**(9), 093402 (2016)

19.132 S. Karkare, D. Dimitrov, W. Schaff, L. Cultrera, A. Bartnik, X. Liu, E. Sawyer, T. Esposito, I. Bazarov: Monte Carlo charge transport and photoemission from negative electron affinity GaAs photocathodes, J. Appl. Phys. **113**(10), 104904 (2013)

19.133 H. Dürr, X. Wang: *Ultrafast Science Opportunities with Electron Microscopy*, Report SLAC-R-1039 (SLAC National Accelerator Laboratory, Stanford 2016)

19.134 S.D. Brorson, J.G. Fujimoto, E.P. Ippen: Femtosecond electronic heat-transport dynamics in thin gold films, Phys. Rev. Lett. **59**(17), 1962 (1987)

19.135 S.I. Anisimov, B.L. Kapeliovich, T.L. Perelman: Electron emission from metal surfaces exposed to ultrashort laser pulses, Zh. Eksp. Teor. Fiz. **66**(776), 375 (1974)

19.136 P.B. Allen: Theory of thermal relaxation of electrons in metals, Phys. Rev. Lett. **59**(13), 1460 (1987)

19.137 Y. Giret, N. Naruse, S.L. Daraszewicz, Y. Murooka, J. Yang, D.M. Duffy, A.L. Shluger, K. Tanimura: Determination of transient atomic structure of laser-excited materials from time-resolved diffraction data, Appl. Phys. Lett. **103**(25), 253107 (2013)

19.138 S.L. Daraszewicz, Y. Giret, N. Naruse, Y. Murooka, J. Yang, D.M. Duffy, A.L. Shluger, K. Tanimura: Structural dynamics of laser-irradiated gold nanofilms, Phys. Rev. B **88**(18), 184101 (2013)

19.139 M.Z. Mo, X. Shen, Z. Chen, R.K. Li, M. Dunning, K. Sokolowski-Tinten, Q. Zheng, S.P. Weathersby, A.H. Reid, R. Coffee, I. Makasyuk, S. Edstrom, D. McCormick, K. Jobe, C. Hast, S.H. Glenzer, X. Wang: Single-shot mega-electronvolt ultrafast electron diffraction for structure dynamic studies of warm dense matter, Rev. Sci. Instrum. **87**(11), 11D810 (2016)

19.140 T. Chase, M. Trigo, A.H. Reid, R. Li, T. Vecchione, X. Shen, S. Weathersby, R. Coffee, N. Hartmann, D.A. Reis, X.J. Wang, H.A. Dürr: Ultrafast electron diffraction from non-equilibrium phonons in femtosecond laser heated Au films, Appl. Phys. Lett. **108**(4), 041909 (2016)

19.141 E.M. Mannebach, R. Li, K.-A. Duerloo, C. Nyby, P. Zalden, T. Vecchione, F. Ernst, A.H. Reid, T. Chase, X. Shen, S. Weathersby, C. Hast, R. Hettel, R. Coffee, N. Hartmann, A.R. Fry, Y. Yu, L. Cao, T.F. Heinz, E.J. Reed, H.A. Dürr, X. Wang, A.M. Lindenberg: Dynamic structural response and deformations of monolayer MoS_2 visualized by femtosecond electron diffraction, Nano Lett. **15**(10), 6889 (2015)

19.142 P.-F. Zhu, F.-C. Fu, L. Sheng-Guang, D. Xiang, J. Zhang, J.-M. Cao: Time-resolved visualization of laser-induced heating of gold with MeV ultrafast electron diffraction, Chin. Phys. Lett. **31**(11), 116101 (2014)

19.143 S. Manz, A. Casandruc, D. Zhang, Y. Zhong, R.A. Loch, A. Marx, T. Hasegawa, L.C. Liu, S. Bayesteh, H. Delsim-Hashemi, M. Hoffmann, M. Felber, M. Hachmann, F. Mayet, J. Hirscht, S. Keskin, M. Hada, S.W. Epp, K. Flottmann, R.J.D. Miller: Mapping atomic motions with ultrabright electrons: Towards fundamental limits in space-time resolution, Faraday Discuss. **177**, 467 (2015)

19.144 P. Zhu, Y. Zhu, Y. Hidaka, L. Wu, J. Cao, H. Berger, J. Geck, R. Kraus, S. Pjerov, Y. Shen, R.I. Tobey, J.P. Hill, X.J. Wang: Femtosecond time-resolved MeV electron diffraction, New J. Phys. **17**(6), 063004 (2015)

19.145 I. Hargittai: Gas-phase electron diffraction for molecular structure determination. In: *Electron Crystallography: Novel Approaches for Structure Determination of Nanosized Materials*, ed. by T.E. Weirich, J.L. Lábár, X. Zou (Springer, Dordrecht 2006) p. 197

19.146 J.C. Williamson, A.H. Zewail: Structural femtochemistry: Experimental methodology, Proc. Natl. Acad. Sci. U.S.A. **88**(11), 5021 (1991)

19.147 J.C. Williamson, A.H. Zewail: Ultrafast electron diffraction. Velocity mismatch and temporal resolution in crossed-beam experiments, Chem. Phys. Lett. **209**(1), 10 (1993)

19.148 J.C. Williamson, J. Cao, H. Ihee, H. Frey, A.H. Zewail: Clocking transient chemical changes by ultrafast electron diffraction, Nature **386**(6621), 159 (1997)

19.149 J. Cao, H. Ihee, A.H. Zewail: Ultrafast electron diffraction and direct observation of transient structures in a chemical reaction, Proc. Natl. Acad. Sci. U.S.A. **96**(2), 338 (1999)

19.150 J. Yang, M. Guehr, T. Vecchione, M.S. Robinson, R. Li, N. Hartmann, X. Shen, R. Coffee, J. Corbett, A. Fry, K. Gaffney, T. Gorkhover, C. Hast, K. Jobe, I. Makasyuk, A. Reid, J. Robinson, S. Vetter, F. Wang, S. Weathersby, C. Yoneda, M. Centurion, X. Wang: Diffractive imaging of a rotational wavepacket in nitrogen molecules with femtosecond megaelectronvolt electron pulses, Nat. Commun. **7**, 11232 (2016)

19.151 J. Yang, M. Guehr, X. Shen, R. Li, T. Vecchione, R. Coffee, J. Corbett, A. Fry, N. Hartmann, C. Hast, K. Hegazy, K. Jobe, I. Makasyuk, J. Robinson, M.S. Robinson, S. Vetter, S. Weathersby, C. Yoneda,

X. Wang, M. Centurion: Diffractive imaging of coherent nuclear motion in isolated molecules, Phys. Rev. Lett. **117**(15), 153002 (2016)

19.152 S.P. Weathersby, G. Brown, M. Centurion, T.F. Chase, R. Coffee, J. Corbett, J.P. Eichner, J.C. Frisch, A.R. Fry, M. Gühr, N. Hartmann, C. Hast, R. Hettel, R.K. Jobe, E.N. Jongewaard, J.R. Lewandowski, R.K. Li, A.M. Lindenberg, I. Makasyuk, J.E. May, D. McCormick, M.N. Nguyen, A.H. Reid, X. Shen, K. Sokolowski-Tinten, T. Vecchione, S.L. Vetter, J. Wu, J. Yang, H.A. Dürr, X.J. Wang: Mega-electron-volt ultrafast electron diffraction at SLAC National Accelerator Laboratory, Rev. Sci. Instrum. **86**(7), 073702 (2015)

19.153 J. Yang, M. Guehr, T. Vecchione, M.S. Robinson, R. Li, N. Hartmann, X. Shen, R. Coffee, J. Corbett, A. Fry, K. Gaffney, T. Gorkhover, C. Hast, K. Jobe, I. Makasyuk, A. Reid, J. Robinson, S. Vetter, F. Wang, S. Weathersby, C. Yoneda, X. Wang, M. Centurion: Femtosecond gas phase electron diffraction with MeV electrons, Faraday Discuss. **194**, 563 (2016)

19.154 X.J. Wang, X. Qiu, I. Ben-Zvi: Experimental observation of high-brightness microbunching in a photocathode RF electron gun, Phys. Rev. E **54**(4), R3121 (1996)

19.155 O. Bostanjoglo: High-speed electron microscopy. In: *Electron Microscopy and Holography*, Advances in Imaging and Electron Physics, Vol. 121, ed. by P.W. Hawkes (Elsevier, Amsterdam 2002) pp. 1–51

19.156 H. Dömer, O. Bostanjoglo: High-speed transmission electron microscope, Rev. Sci. Instrum. **74**(10), 4369 (2003)

19.157 T. LaGrange, M.R. Armstrong, K. Boyden, C.G. Brown, G.H. Campbell, J.D. Colvin, W.J. DeHope, A.M. Frank, D.J. Gibson, F.V. Hartemann, J.S. Kim, W.E. King, B.J. Pyke, B.W. Reed, M.D. Shirk, R.M. Shuttlesworth, B.C. Stuart, B.R. Torralva, N.D. Browning: Single-shot dynamic transmission electron microscopy, Appl. Phys. Lett. **89**(4), 044105 (2006)

19.158 J.S. Kim, T. LaGrange, B.W. Reed, M.L. Taheri, M.R. Armstrong, W.E. King, N.D. Browning, G.H. Campbell: Imaging of transient structures using nanosecond in situ TEM, Science **321**(5895), 1472 (2008)

19.159 A.H. Zewail: Four-dimensional electron microscopy, Science **328**(5975), 187 (2010)

19.160 A. Rose: Television pickup tubes and the problem of vision, Adv. Electron. Electron Phys. **1**, 131 (1948)

19.161 B.W. Reed, M.R. Armstrong, N.D. Browning, G.H. Campbell, J.E. Evans, T. LaGrange, D.J. Masiel: The evolution of ultrafast electron microscope instrumentation, Microsc. Microanal. **15**(4), 272 (2009)

19.162 J.C.H. Spence, G. Subramanian, P. Musumeci: Hollow cone illumination for fast TEM, and outrunning damage with electrons, J. Phys. B **48**(21), 214003 (2015)

19.163 R.F. Egerton, P. Li, M. Malac: Radiation damage in the TEM and SEM, Micron **35**(6), 399 (2004)

19.164 D.H. Dowell, M. Ferrario, T. Kimura, J. Lewellen, C. Limborg, P. Raimondi, J.F. Schmerge, L. Serafini, T. Smith, L. Young: A two-frequency RF photocathode gun, Nucl. Instrum. Methods Phys. Res. A **528**(1), 316 (2004)

19.165 J.C.H. Spence: *High-Resolution Electron Microscopy* (Oxford Univ. Press, Oxford 2013)

19.166 J.K. Lim, P. Frigola, G. Travish, J.B. Rosenzweig, S.G. Anderson, W.J. Brown, J.S. Jacob, C.L. Robbins, A.M. Tremaine: Adjustable, short focal length permanent-magnet quadrupole based electron beam final focus system, Phys. Rev. ST Accel. Beams **8**(7), 072401 (2005)

19.167 D. Cesar, J. Maxson, P. Musumeci, Y. Sun, J. Harrison, P. Frigola, F.H. O'Shea, H. To, D. Alesini, R.K. Li: Demonstration of single-shot picosecond time-resolved MeV electron imaging using a compact permanent magnet quadrupole based lens, Phys. Rev. Lett. **117**(2), 024801 (2016)

19.168 L. Cultrera, S. Karkare, H. Lee, X. Liu, I. Bazarov, B. Dunham: Cold electron beams from cryocooled, alkali antimonide photocathodes, Phys. Rev. ST Accel. Beams **18**, 113401 (2015)

19.169 T. Shibuya, N. Hayashizaki, M. Yoshida: Fabrication of two dimensional nano-scale photocathode arrays in transparent conductor for high coherence beam generation. In: *Proc. Int. Part. Accel. Conf. IPAC'16* (2016) p. WEPMY040

19.170 H. Lee, L. Cultrera, I. Bazarov: Intrinsic emittance reduction in transmission mode photocathodes, Appl. Phys. Lett. **108**(12), 124105 (2016)

19.171 F. Carbone, B. Barwick, O.H. Kwon, H.S. Park, J.S. Baskin, A.H. Zewail: EELS femtosecond resolved in 4-D ultrafast electron microscopy, Chem. Phys. Lett. **468**, 107 (2009)

19.172 F. Carbone, O.H. Kwon, A.H. Zewail: Dynamics of chemical bonding mapped by energy-resolved 4-D electron microscopy, Science **325**, 181 (2009)

19.173 L. Piazza, C. Ma, H.X. Yang, A. Mann, Y. Zhu, J.Q. Li, F. Carbone: Ultrafast structural and electronic dynamics of the metallic phase in a layered manganite, Struct. Dyn. **1**, 014501 (2014)

19.174 D.A. Plemmons, S.T. Park, A.H. Zewail, D.J. Flannigan: Characterization of fast photoelectron packets in weak and strong laser fields in ultrafast electron microscopy, Ultramicroscopy **146**, 97 (2014)

19.175 R.M. van der Veen, T.J. Penfold, A.H. Zewail: Ultrafast core-loss spectroscopy in 4-D electron microscopy, Struct. Dyn. **2**, 024302 (2015)

19.176 A. Feist, K.E. Echternkamp, J. Schauss, S.V. Yalunin, S. Schäfer, C. Ropers: Quantum coherent optical phase modulation in an ultrafast transmission electron microscope, Nature **521**, 200 (2015)

19.177 R.F. Egerton: *Electron Energy-Loss Spectroscopy in the Electron Microscope*, 3rd edn. (Springer, New York 2011)

19.178 R.K. Li, X.J. Wang: Femtosecond mega-electron-volt electron energy-loss spectroscopy, Phys. Rev. Appl. **8**, 054017 (2017)

19.179 F. Fu, S. Liu, P. Zhu, D. Xiang, J. Zhang, J. Cao: High quality single shot ultrafast MeV electron diffraction from a photocathode radio-frequency gun, Rev. Sci. Instrum. **85**(8), 083701 (2014)

19.180 L.K. Rudge, S. Mathisen, P. Aden, R.J. Cash, J.A. Clarke, D.M.P. Holland, J.W. McKenzie, M.D. Roper, T.C.Q. Noakes, J. Jones, A. Kalinin, B.L. Militsyn, B.D. Muratori, D. Scott, F. Jackson, P. Williams, Y. Saveliev, D. Angal-Kalinin, M. Surman, D.A. Wann, P.D. Lane, J.G. Underwood: Single shot multi MeV ultrafast electron diffraction at VELA. In: *Proc. IPAC2014* (2014) p. TUPW1017

19.181 S. Setiniyaz, H.W. Kim, I.-H. Baek, J. Nam, M. Chae, B.-H. Han, B. Gudkov, K.H. Jang, S. Park, Y.U. Jeong, S. Miginsky, N. Vinokurov: Beam characterization at the KAERI UED beamline, J. Korean Phys. Soc. **69**(6), 1019 (2016)

Pietro Musumeci

Dept. of Physics & Astronomy
University of California at Los Angeles
Los Angeles, CA, USA
musumeci@physics.ucla.edu

Pietro Musumeci is the director of the UCLA Pegasus Lab. His interests lie in the application of ultrafast high-power laser technologies to accelerators and beam physics. He was elected APS Fellow in 2017 for his contributions in laser acceleration, photoinjector, and high-brightness beam production. His recent work has focused on developing novel time-resolved electron scattering techniques based on ultrashort relativistic electrons.

Renkai Li

SLAC National Accelerator Laboratory
Menlo Park, CA, USA
lrk@slac.stanford.edu

Renkai Li received his PhD from Tsinghua University in 2010. He has worked at the University of California, Los Angeles, and at the SLAC National Accelerator Laboratory. His work is in the area of accelerator and beam physics, and focuses on the physics and technology of new electron sources and bright electron beams, as well as their application in ultrafast electron scattering.